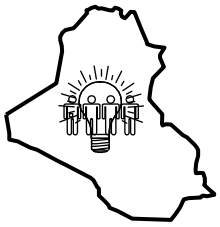

SPONSORED AND PUBLISHED BY
THE IRAQI SOCIETY FOR ALTERNATIVE AND RENEWABLE ENERGY SOURCES AND TECHNIQUES (I.S.A.R.E.S.T.)

EDITORIAL BOARD

ADVISORY BOARD

Organized by I.S.A.R.E.S.T.

INVITATION TO ATTEND

To introduce more about the alternative and renewable energy sources and techniques, **I.S.A.R.E.S.T.** invites you to attend a scientific lecture at the School of Applied Sciences, University of Technology. You are requested to contact the **I.S.A.R.E.S.T.** secretary and register your attendance. The lecture will be held earlier due to the registered requests.
To introduce more about environment and how to protect from contamination and pollution, **I.S.A.R.E.S.T.** invites you to attend a scientific lecture on the environment protection. The lecturer is **Dr. Isam K. Al-Rawi**. You are requested to contact the **I.S.A.R.E.S.T.** secretary and register your attendance. The lecture will be held earlier due to the registered requests.

INVITATION TO PARTICIPATE

To all they would like to submit seminars or scientific lectures during the first semester of the **I.S.A.R.E.S.T.** (January, February and March) in 2006, you are kindly requested to contact the secretary of the **I.S.A.R.E.S.T.** for date and presentation arrangements of the seminars or lectures. Please, do not hesitate to participate in our activities, this chance might be required by young scientists in our country, IRAQ, to develop and grow as well as introduce the professors and experts in field. You could find us on the post address, emails and mobile below:

Postal:
P. O. Box 55259, Baghdad 12001, IRAQ

Emails:
irq_appl_phys@yahoo.com
editor_ijap@yahoo.com
odayata2001@yahoo.com

Mobile:
00964-1-7901274190

If you would like to meet us, we would so too. You could visit us in Laser Research Unit, University of Technology, Baghdad, IRAQ. You could meet

- **Dr. Raad A. KHAMIS**
- **Dr. Akram N. MUHAMMAD**
- **Dr. Adawiya J. HAIDER**

Also, you could visit **Dr. Raad S. Al-Rawi** at Department of Physics, College of Science, Al-Mustansiriya University, Baghdad, IRAQ.

Walid K. Hamoudi [1]
Raid A.W. Ismail [2]
Ra'ad S. Abid [3]
Munaf R. Ismail [1]

1 School of Applied Sciences, University of Technology, Baghdad, IRAQ
2 Physics Science and Research Center, Ministry of Science and Technology, Baghdad, IRAQ
3 Department of Physics, College of Science, Al-Mustansiriya University, Baghdad, IRAQ

Wideband (0.6-11) micron Angle Deposited Thin Te:S Laser Detector

A study of nanostructural, optical and electrical characteristics of obliquely deposited thin sulfur-doped films is presented. The aim was to develop a wideband (0.6-11)μm laser detector operating at room temperature with no need to biasing or amplification. The deposition angle had a decisive role on the detector specifications, namely its detectivity and response time. At deposition angle of θ=70°, the maximum detectivity was achieved, $D^*=3x10^9$ $W^{-1}.Hz^{1/2}.cm$ while at θ=60° a fastest response $\tau_s=1\mu s$ was obtained.

Keywords: *Laser detector, Angle deposition, Te devices, Nanostructure*

Received: 11 August 2005, Revised: 7 September 2005, Accepted: 30 September 2005

1. Introduction

The principal growth parameters of thin films are substrate type and its temperature, vaporization temperature, vapor deposition angle, pressure of contaminating gases, vacuum pressure and the rate of deposition [1]. The adsorption of gaseous atoms leads to a small grain crystalline growth of a size that could increase when substrate temperature rises as this reduces the lattice defects [2]. The structure of the thin tellurium films depends largely on the deposition conditions [3]. The grain growth increases with the deposition rate and substrate temperature. When deposited on a pre-heated (125-200)°C glass substrate, the tellurium showed needle structure along the substrate plane [4]. The dimensions of this needle structure were proportional to deposition rate. Tellurium grain size increased with the film thickness.

An angle deposition of a thin film can form a structure with high density of rods or needles separated by low density voids [5,6] but band gap is independent of the angle [7]. When depositing at an angle, the thin film density decreases with increasing the angle [8,9] and the columnar growth formation depends on the geometrical shadowing where incident atoms are blocked by previously deposited atoms. Self shadowing effect increases when decreasing atomic mobility and this effect can produce nanorods tilted toward the incident deposition flux [10]. To limit or prevent columnar growth, the substrate temperature needs to be increased during the deposition process to allow for some grain growth and re-crystallization [9]. The effect of angle deposition on structural and magnetic properties of e-beam evaporated Co/Pt multilayer thin films prepared on tilted substrates was examined [11]. It was found that the [111] crystallographic orientations of these multilayer films where not aligned with the columnar growth orientations. The integration of various morphologies generated by dynamic angle deposition to produce zigzag, helical and cylindrical columns was performed. A uniform and flat layer was formed on porous layers by a gradual change in the deposition geometry [12]. Shape related physical anisotropies and chemical activity due to high porosity were integrated in one thin film to be used in solar cells and chemical sensors applications. When increasing the substrate temperature to a certain value, all voids can disappear and the film becomes homogeneous [5]. The columnar growth axis direction makes an angle (β) with the normal to the substrate, and in most cases ($\beta<\theta$) where θ is the deposition angle. These two angles are correlated as [13]:

$$2 \tan \beta = \tan \theta \qquad (1)$$

Angular deposition shows asymmetrical properties in the film plane. In this type of deposition the asymmetry and the surface area increase, and so do the columns separation, with increasing the angle θ. For Te thin films, the angle β has a large dependence on θ for thickness greater than 80nm. This dependency decreases when increasing the substrate temperature during deposition [14].

Angle deposited thin Te films are used as good absorbing surfaces due to their self-shadowing property. The geometry of these surfaces allows excellent absorption of the sun

spectrum through multiple reflections. Fig. (1) shows the effect of varying the deposition angle on absorptivity of thin Te films [15]. As seen, 95% absorptivity was obtained at θ=80°. The 0.37eV energy gap of Te is a favorable value to prepare high absorptivity surface for visible spectrum. Tellurium films are p-type semiconductor with a conductivity increases with deposition rate [16-18]. A temperature gradient (dT/dx) in a thin film material produces a potential gradient (dV/dx). The ratio between them, i.e., the e.m.f (ΔV) per temperature difference (ΔT) across the opposite sides of a thin film is the thermoelectric power given by:

$$S = \frac{\Delta V}{\Delta T} \qquad (2)$$

The highest e.m.f is obtained when the film thickness is greater than 250nm [19]. The thermoelectric behavior of thin films depends on conduction mechanism of free electrons in the film. For metallic films, the thermoelectric power (S) is given as [20]:

$$S = -\frac{\pi^2 k_B^2 T}{3e}\left[\frac{1}{\sigma}\frac{d\sigma}{dE}\right]_{E=E_F} \qquad (3)$$

where σ is conductivity of the film, E and E_F are electron and Fermi energies, respectively, T is the temperature, e is the absolute value of electronic charge and k_B is Boltzman constant.

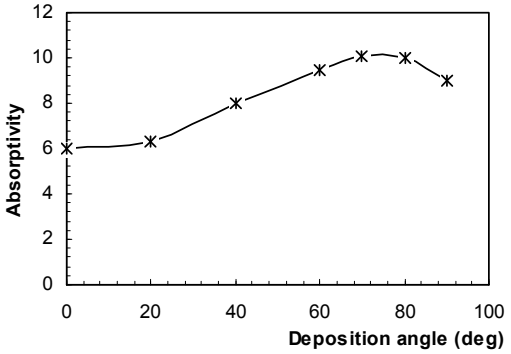

Fig. (1): Absorptivity *vs.* deposition angle of thin Te:S film [15]

The relationship between S and $1/T$ for Te thin films was presented [17]. The curves showed linear relation only at low temperature ranges and saturated at high temperature.

Thin films of some materials exhibit potential difference across their length when obliquely deposited. Anisotropic stresses are created which induces an e.m.f when illuminated by laser pulses. The deposition angle plays an important role the film resistance and consequently, on the value of the generated e.m.f [21]. Cadmium telluride (CdTe) thin films deposited at θ=21° produced an e.m.f when illuminated by a continuous light. The microstructural study showed grains about the size of the film thickness [22]. The sensitivity of these films and their characteristics greatly depended on deposition angle and substrate temperature.

2. Experiment

High optical quality glass slides were used as substrates. They were firstly cleaned by alcohol then by HCl acid for 15 seconds, rinsed afterwards in deionized water and finally cleaned again by alcohol in an ultrasonic bath for 10 minutes. Thin Te:S films were thermally evaporated on the glass substrates for a range of angles (0-80°). Ohmic contacts were then performed by evaporating a thin layer of high purity (99.999%) aluminum on the opposite sides of the films. Three pulsed lasers; ruby, Nd:YAG and CO_2, were used to test the performance of the films prepared as pulsed laser detectors.

3. Results and Discussion

3.1 X-ray Studies

Figure (2) shows an x-ray diffraction spectrum for Te:S thin films deposited at different angles. The films have a polycrystalline structure. The reflection intensities increased from their values at the (100) plane when varying the deposition angle by a little amount but start to decrease at large angles. In general, the reflection intensity is a decreasing function of the deposition angle. Table (1) summarizes the x-ray diffraction results for the obliquely deposited Te:S films.

3.2 Heat Treatment Effect on X-ray Diffraction Studies

Figures (3) and (4) show the x-ray diffraction results for Te:S thin films deposited at (θ=0-70°) and thermally treated for 15 minutes. At T=50°C and θ=0°, the reflection intensities from the (100), (110), (200) and (210) planes decreased while those from the (101) and (201 increased with an appearance of new reflection peaks at (102), (111), (202) and (113) and disappearance of the peak originally existed at the (211) plane. Further increase of thermal treatment temperature has lowered some peaks and raised others, see Table (2). At θ=70°, a polycrystalline structure and an oscillation of the peak intensity reflections resulted as presented in Table (3).

3.3 SEM Studies

Figure (5) shows the SEM from the surfaces of the obliquely deposited Te:S thin films. Columnar nano-scale growth is very clear in the structure. This material has a great tendency to form self shadowing. The structure reveals intense nanorods separated by deep vacancies, both are responsible for the surface roughness.

The size of these nanostructure rods was within the range of (100-400) nm.

Table (1) X-ray diffraction results for Te:S thin films deposited at different angles at room temperature, together with the ASTM values

θ°	2ϕ°	d (Å)	(hkl)	I/I_1 (XRD)	I/I_1 (ASTM)
0	**29.1**	**3.86**	**(100)**	**62**	**20**
	34.9	3.23	(101)	21	100
	51.5	2.229	(110)	33	31
	60.2	1.93	(200)	10	4
	63.7	1.835	(201)	5	20
	83.2	1.459	(210)	10	8
	86.2	1.417	(211)	4	8
10	**29.1**	**3.86**	**(100)**	**84**	**20**
	34.9	3.23	(101)	27	100
	51.5	2.229	(110)	33	31
	60.2	1.93	(200)	9	4
	63.7	1.835	(201)	7	20
20	**29.1**	**3.86**	**(100)**	**54**	**20**
	34.9	3.23	(101)	23	100
	51.5	2.229	(110)	34	31
	60.2	1.93	(200)	6	4
	63.7	1.835	(201)	6	20
	83.2	1.459	(210)	6	8
30	**29.1**	**3.86**	**(100)**	**59**	**20**
	34.9	3.23	(101)	21	100
	51.5	2.229	(110)	31	31
	55.3	2.087	(111)	6	11
	60.2	1.93	(200)	5	4
40	**29.1**	**3.86**	**(100)**	**37**	**20**
	34.9	3.23	(101)	7	100
	51.5	2.229	(110)	20	31
	60.2	1.93	(200)	7	4
	63.7	1.835	(201)	4	20
50	**29.1**	**3.86**	**(100)**	**20**	**20**
	34.9	3.23	(101)	18	100
	51.5	2.229	(110)	14	31
	55.3	2.087	(111)	57	11
	58.6	1.98	(003)	8	8
	63.7	1.835	(201)	5	20
60	**29.1**	**3.86**	**(100)**	**15**	**20**
	34.9	3.23	(101)	8	100
	51.5	2.229	(110)	8	31

3.4 Absorption Studies

For the spectral range 0.4–2μm, optical glass substrates were used whereas ZnSe substrates were chosen for 2-12μm. the absorptivity decreased with increasing wavelength but increased at large deposition angles due to the increased surface area of the films. Large θ enhances self shadowing which helps the formation of columnar growth [6,15,23]. The nanorods separation increases and so does the surface area [6,15], see Fig. (6) and Fig. (7). The effect of thermal heat treatment of the Te:S films was considered and Figures (8-11) show this effect. At θ=0, the absorptivity did not change much with the annealing temperature but its value was decreasing with the wavelength of the incident light. At θ=70°, the general behavior was the same with some increase in absorptivity at short wavelengths.

The absorption coefficient (α) was calculated using the relation [24,25]:

$$\alpha = \frac{1}{t}\ln\left(\frac{1-R}{T}\right) \qquad (4)$$

where T is the transmission, t is the thin film thickness and R is the thin film reflectivity.

The absorption coefficient (α) was an increasing function of the deposition angle, see Fig. (12) and Fig. (13), but its value was decreasing at longer wavelengths.

Table (2) X-ray diffraction results for Te:S thin films deposited at 0° on glass substrate and thermally treated, together with the ASTM values

T (°C)	2ϕ°	d (Å)	(hkl)	I/I_1 (XRD)	I/I_1 (ASTM)
50	**29.1**	**3.86**	**(100)**	**38**	**20**
	34.9	3.23	(101)	77	100
	48.7	2.35	(102)	12	37
	51.5	2.229	(110)	28	31
	55.3	2.087	(111)	5	11
	60.2	1.93	(200)	3	4
	63.7	1.835	(201)	10	20
	73.6	1.617	(202)	4	12
	81.8	1.479	(113)	2	13
	83.2	1.459	(210)	4	8
100	**29.1**	**3.86**	**(100)**	**34**	**20**
	34.9	3.23	(101)	89	100
	48.7	2.35	(102)	13	37
	51.5	2.229	(110)	29	31
	55.3	2.087	(111)	6	11
	60.2	1.93	(200)	8	4
	63.7	1.835	(201)	11	20
	65.9	1.781	(112)	3	7
	73.6	1.617	(202)	4	12
	81.8	1.479	(113)	3	13
150	**29.1**	**3.86**	**(100)**	**32**	**20**
	34.9	3.23	(101)	100	100
	48.7	2.35	(102)	16	37
	51.5	2.229	(110)	24	31
	55.3	2.087	(111)	7	11
	60.2	1.93	(200)	3	4
	63.7	1.835	(201)	12	20
	65.9	1.781	(112)	4	7
	73.6	1.617	(202)	4	12
	81.8	1.479	(113)	3	13
200	**29.1**	**3.86**	**(100)**	**42**	**20**
	34.9	3.23	(101)	93	100
	48.7	2.35	(102)	13	37
	51.5	2.229	(110)	40	31
	55.3	2.087	(111)	6	11
	60.2	1.93	(200)	4	4
	63.7	1.835	(201)	12	20
	65.9	1.781	(112)	2	7
	73.6	1.617	(202)	4	12
	81.8	1.479	(113)	3	13
250	**29.1**	**3.86**	**(100)**	**55**	**20**
	34.9	3.23	(101)	82	100
	48.7	2.35	(102)	11	37
	51.5	2.229	(110)	66	31
	55.3	2.087	(111)	7	11
	58.6	1.98	(003)	1	8
	60.2	1.93	(200)	6	4
	63.7	1.835	(201)	12	20
	65.9	1.781	(112)	1	7
	73.6	1.617	(202)	4	12
	81.8	1.479	(113)	2	13

3.5 Seebeck Coefficient Results

The relation between Seebeck coefficient (*S*) and temperature for 350nm obliquely deposited thin Te:S film is shown in Fig. (14). The Seebeck coefficient (*S*) has positive value which increases with temperature difference (ΔT) for all deposition angles. This is in a good agreement with others [17]. Values of the coefficient *S* are in the range 80-320μV/K depending on temperature and deposition angle.

Table (3) X-ray diffraction results for Te:S thin films deposited at 70° on glass substrate and thermally treated, together with the ASTM values

T (°C)	2ϕ °	*d* (Å)	(*hkl*)	I/I_1 (XRD)	I/I_1 (ASTM)
0	**29.1**	**3.86**	**(100)**	**18**	**20**
	34.9	3.23	(101)	31	100
	48.7	2.35	(102)	8	37
	51.5	2.229	(110)	9	31
	55.3	2.087	(111)	1	11
	58.6	1.98	(003)	1	8
	60.2	1.93	(200)	2	4
	63.7	1.835	(201)	3	20
	73.6	1.617	(202)	1	12
100	**29.1**	**3.86**	**(100)**	**28**	**20**
	34.9	3.23	(101)	43	100
	48.7	2.35	(102)	10	37
	51.5	2.229	(110)	12	31
	55.3	2.087	(111)	2	11
	58.6	1.98	(003)	1	8
	60.2	1.93	(200)	2	4
	63.7	1.835	(201)	4	20
	73.6	1.617	(202)	2	12
150	**29.1**	**3.86**	**(100)**	**22**	**20**
	34.9	3.23	(101)	36	100
	48.7	2.35	(102)	9	37
	51.5	2.229	(110)	11	31
	55.3	2.087	(111)	2	11
	60.2	1.93	(200)	1	4
	63.7	1.835	(201)	3	20
	65.9	1.781	(112)	1	7
	73.6	1.617	(202)	2	12
200	**29.1**	**3.86**	**(100)**	**25**	**20**
	34.9	3.23	(101)	33	100
	48.7	2.35	(102)	8	37
	51.5	2.229	(110)	11	31
	55.3	2.087	(111)	2	11
	60.2	1.93	(200)	2	4
	63.7	1.835	(201)	3	20
	65.9	1.781	(112)	1	7
	73.6	1.617	(202)	1	12

Table (4) Aging factor measurements for Te:S thin film detectors

Detector	Responsivity		
	After 2 months (μV/W)	After 4 months (μV/W)	After 1 year (μV/W)
Te	24	24	24
Te:S	28	27.5	28

3.6 Thin Film Properties under Illumination

Figure (15) shows the photocurrent generated under different illumination optical powers for a range of Te:S film thicknesses. It shows a good linear behavior up to a film thickness of 250nm. The responsivity of these films was ~162μA/W for white light illumination. The small percentage of sulfur (1%) helps absorbing the recombination centers, offsetting the surface defects and as a result increasing the thermoelectric coefficient. Figure (16) is a plot of the responsivity curve at different depositing angles under ambient conditions when illuminated by a pulsed ruby laser. A maximum responsivity of 5mV/W was obtained at θ=70°. For pure Te films, the maximum responsivity was 2.8mV/W at the same deposition angle. Surface study for the Te:S thin film detector showed no damage or saturation after being illuminated by 1kW ruby laser pulses. This reveals the ability of these detectors to withstand high incident optical power with no need of using attenuators. Figure (17) shows the output ruby laser pulse registered by Te:S detectors prepared at θ=70°. The temporal structure on the pulse envelope indicates higher speed of response than the Te thin film detector. Figure (18) shows the value of responsivity as a function of the deposition angle when illuminating the Te:S detector with an Nd:YAG laser pulse. The highest responsivity achieved was 0.1V/W at θ=70°. For Te thin film detector, the responsivity was 0.08V/W. Figure (19) shows an output pulse from a 25mJ Nd:YAG laser caught by Te:S thin film detector deposited at θ=70°. Figure (20) is the output laser pulse caught by the Te thin film detector deposited at θ=70° after being illuminated by the same pulsed Nd:YAG laser. Figure (21) shows the responsivity measurements for the Te and Te:S thin film detectors. They gave 24mV/W and 28mV/W, respectively, after being illuminated by 200ns pulses from a CO_2 laser. The aging factor was considered to study the performance of the Te:S and Te thin film detectors, as indicated in Table (4). Their performance was extremely stable with time. Figure (22) is a photograph of the 200ns pulse from CO_2 laser registered by the Te:S thin film detector.

3.7 Responsivity Homogeneity of the Obliquely Deposited Thin Te Detectors

This parameter is important for detectors having large area like ours (10mmx60mm) or when the beam spot size is very small compared to the sensitive area. Figure (23) shows the generated e.m.f after Nd:YAG laser pulse illumination at different positions from the ohmic contacts of the Te:S thin film deposited at θ=70°. For a film thickness of 100nm, the homogeneous operating region starts from a distance of 20mm from the ohmic contacts. The homogeneous region, however, started from 6mm from the contacts when a film thickness of 350nm was used.

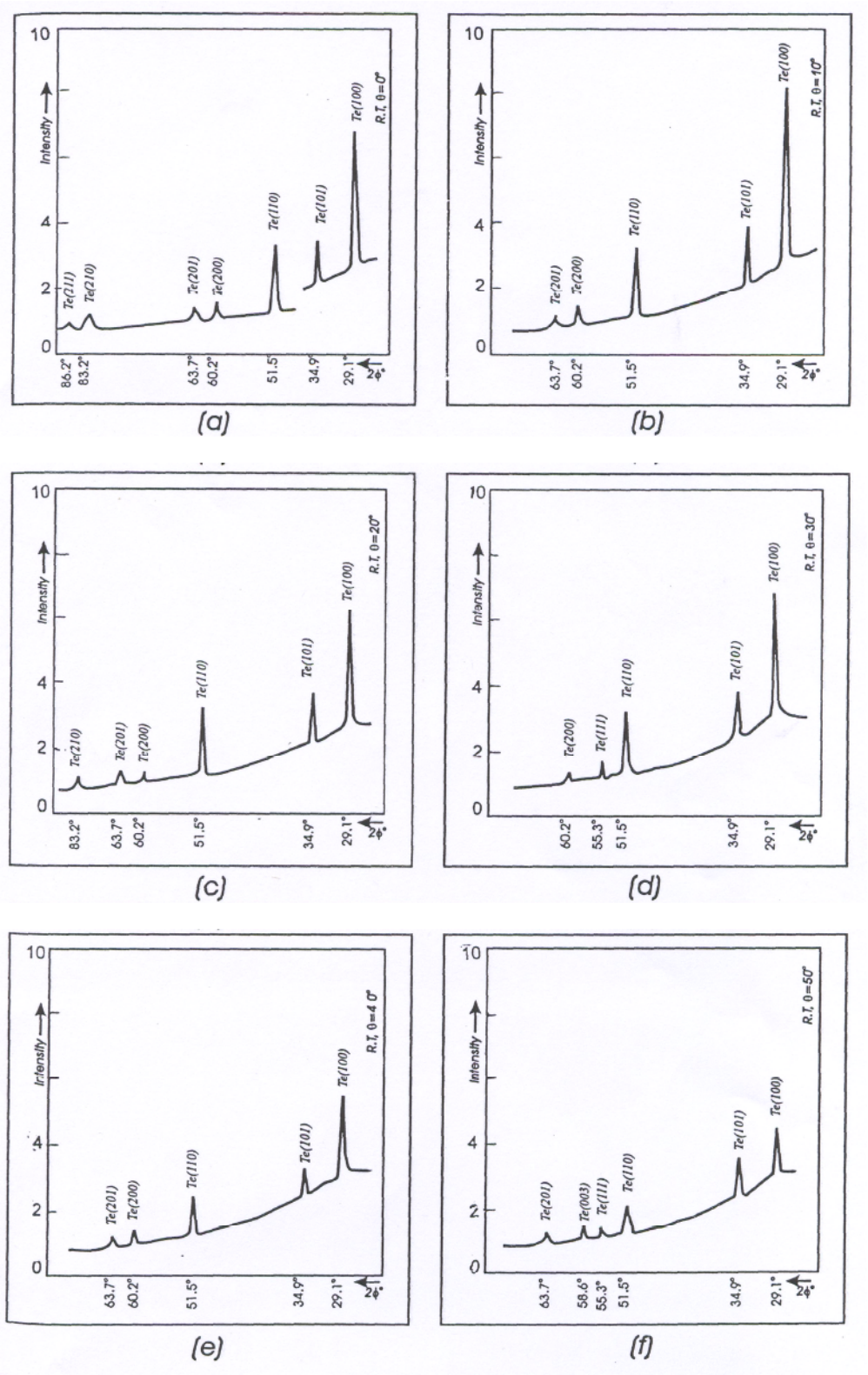

Fig. (2): X-ray diffraction analysis for thin Te:S films deposited at different angles

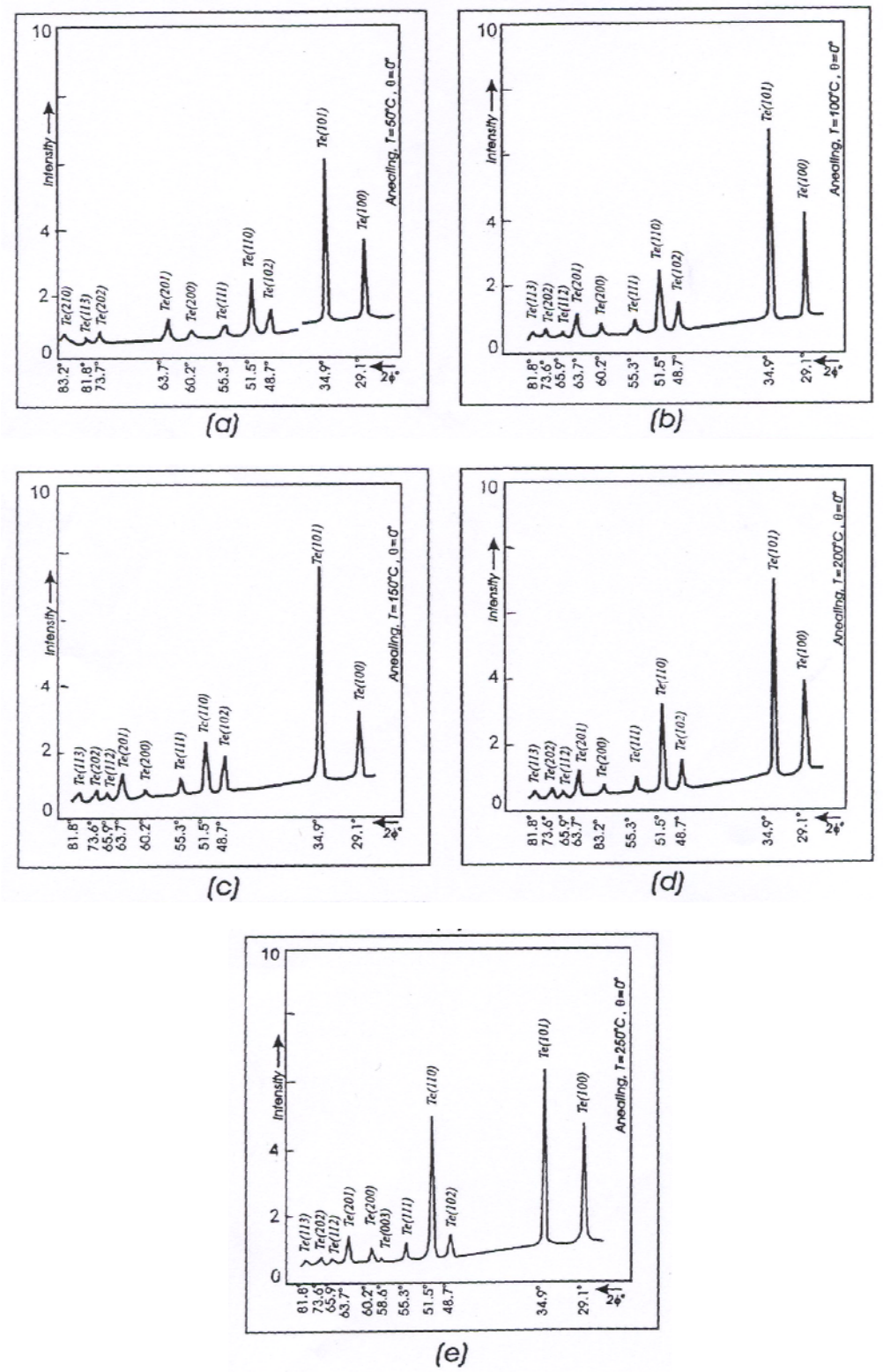

Fig. (3): X-ray diffraction analysis for thin Te:S films deposited at θ=0° and thermally treated

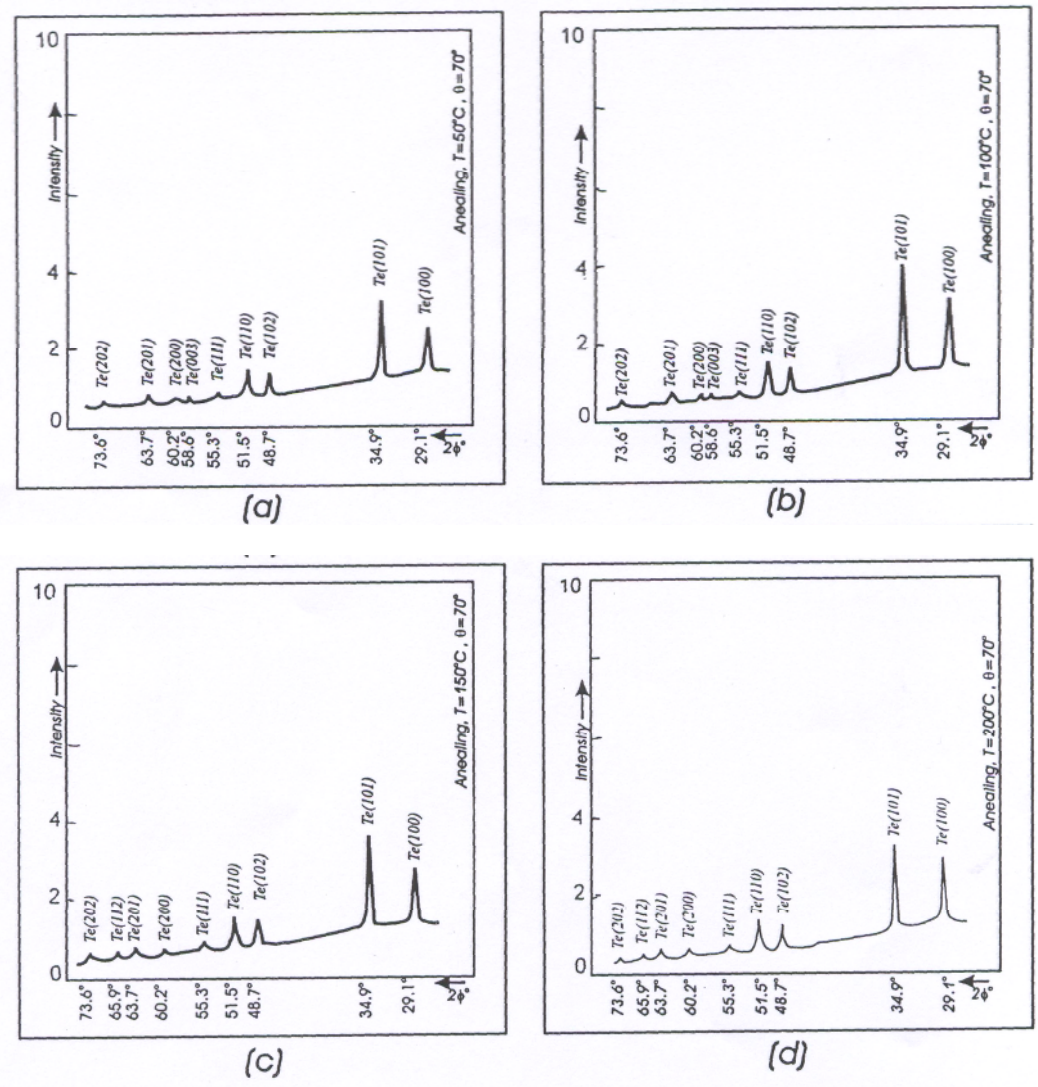

Fig. (4): X-ray diffraction analysis for thin Te:S films deposited at θ=70° and thermally treated

3.8 Noise Current Measurements

Figure (24) is a variation of the noise current with the deposition angle for both Te and Te:S thin film detectors. Noise current was a decreasing function of the deposition angle. This is attributed to the increased resistivity of the films at large angles as a result of columnar growth and anisotropic stress in the film structure. The Te:S detector had lower noise current than that of the Te detectors.

3.9 Specific Detectivity Measurements (D^*)

Figure (25) shows the values of the specific detectivity (D^*) for different wavelengths at room temperature. The figure shows that the performance of Te:S detector is better than the pure tellurium detector. Specific detectivity was a decreasing function of the wavelength and a value of $3x10^9 W^{-1}.Hz^{1/2}.cm$ was obtained when detecting a ruby laser pulses. A comparable reading was achieved when detecting an Nd:YAG laser pulses. For CO_2 laser pulse, the value of D^* was 10^6 $W^{-1}.Hz^{1/2}.cm$.

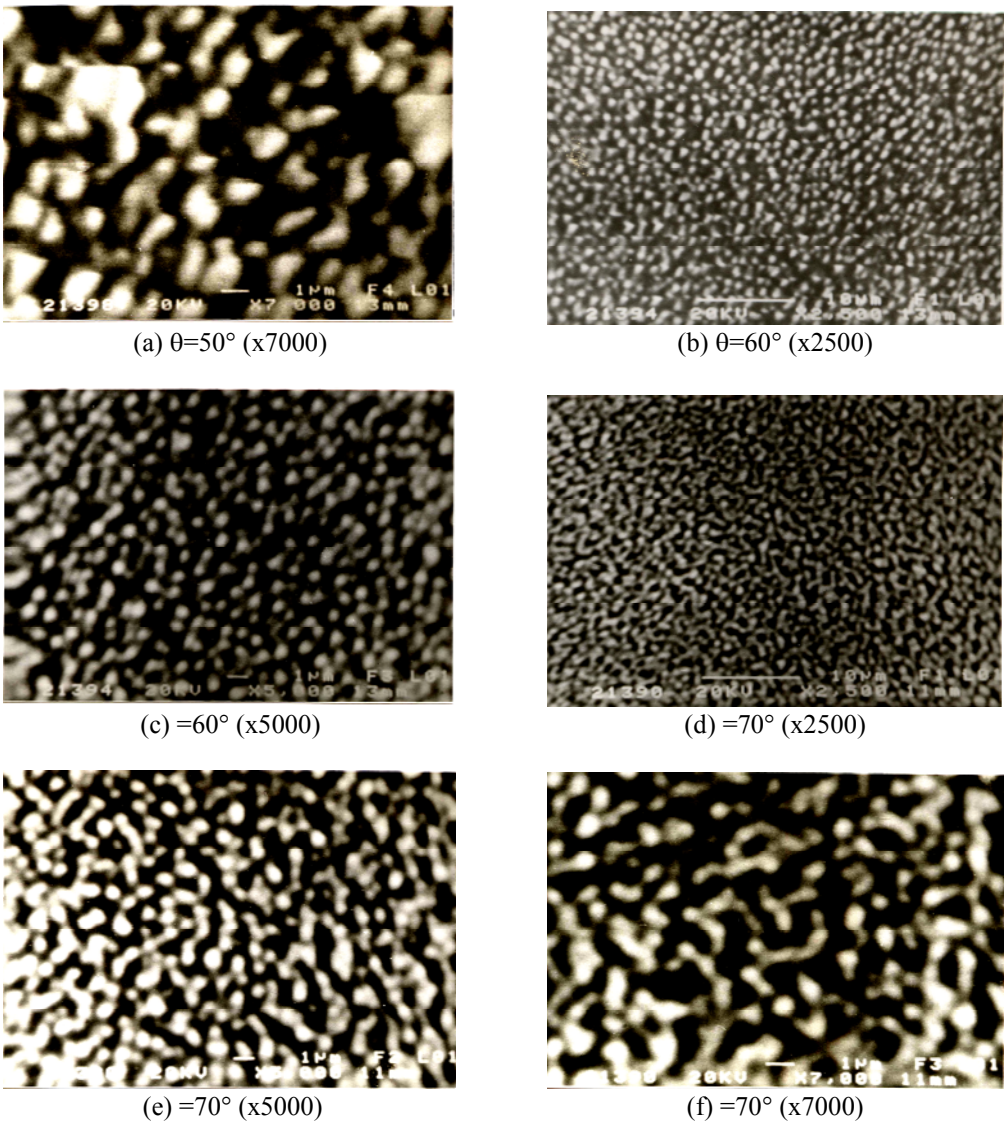

(a) θ=50° (x7000) (b) θ=60° (x2500)

(c) =60° (x5000) (d) =70° (x2500)

(e) =70° (x5000) (f) =70° (x7000)

Fig. (5): Surface study of thin Te:S films deposited at different angles

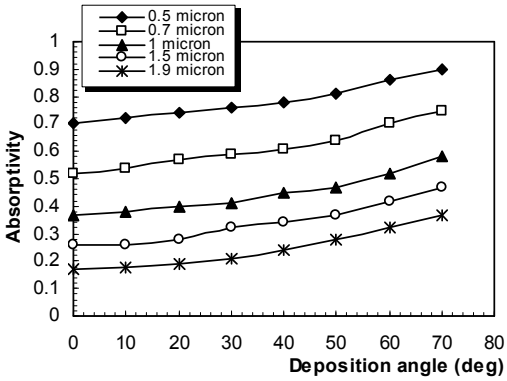

Fig. (6): Absorptivity *vs.* deposition angle for thin Te:S films deposited at room temperature

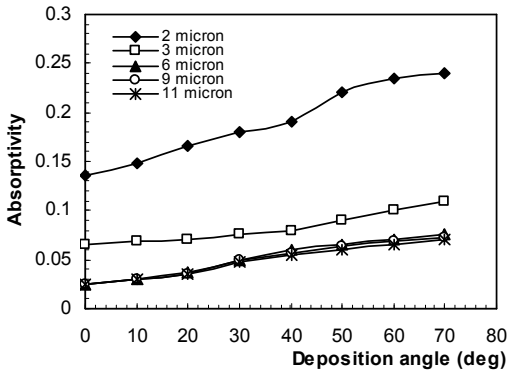

Fig. (7): Absorptivity *vs.* deposition angle for thin Te:S films deposited at different wavelengths

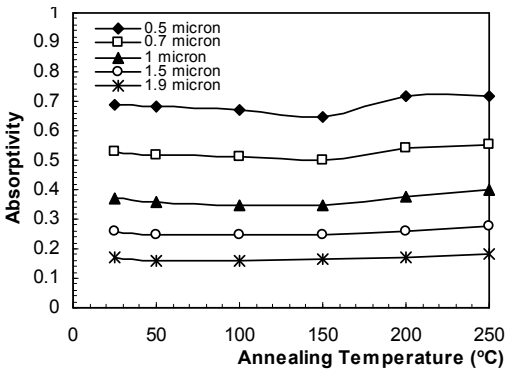

Fig. (8): Absorptivity *vs.* treatment temperature for thin Te:S films deposited at θ=0°

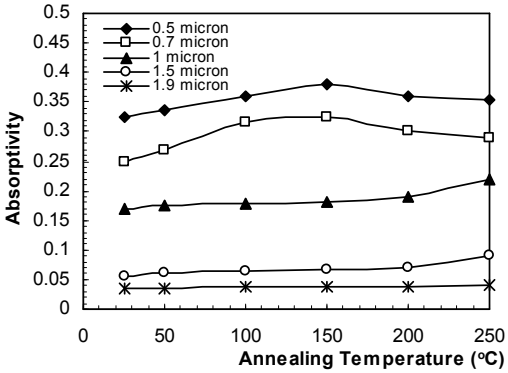

Fig. (9): Absorptivity *vs.* treatment temperature for thin Te:S films deposited at θ=70°

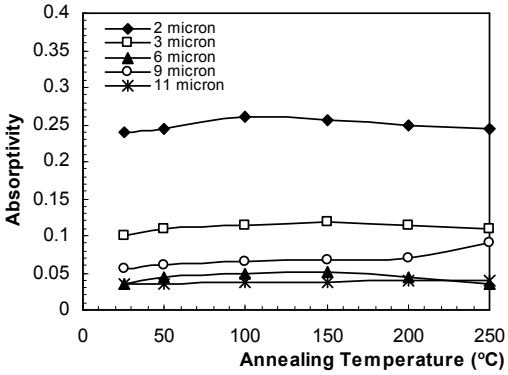

Fig. (10): Absorptivity *vs.* treatment temperature for thin Te:S films deposited at θ=0° on ZnSe substrates

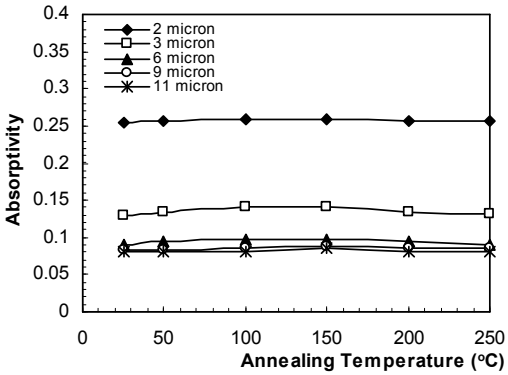

Fig. (11): Absorptivity *vs.* treatment temperature for thin Te:S films deposited at θ=70° on ZnSe substrates

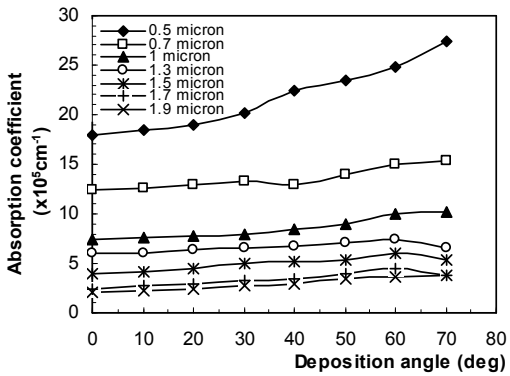

Fig. (12): Absorption coefficient *vs.* deposition angle for thin Te:S films deposited at room temperature

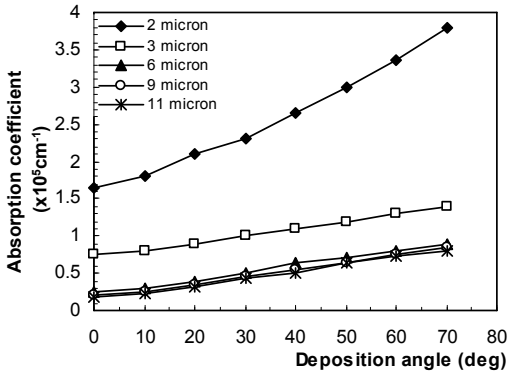

Fig. (13): Absorption coefficient *vs.* deposition angle for thin Te:S films deposited at different wavelengths

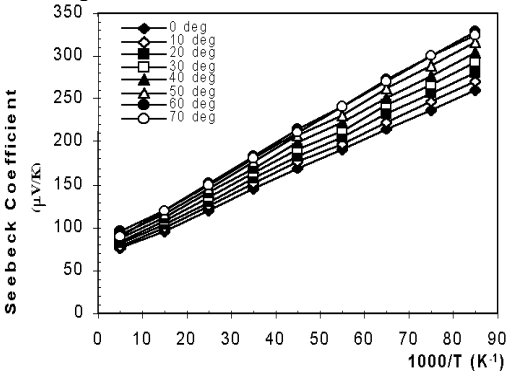

Fig. (14): Seebeck coefficient *vs.* temperature of the thin Te:S films deposited at different angles

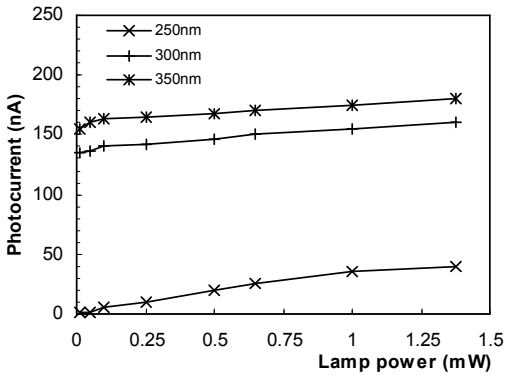

Fig. (15): The linear characteristics of the Te:S detector

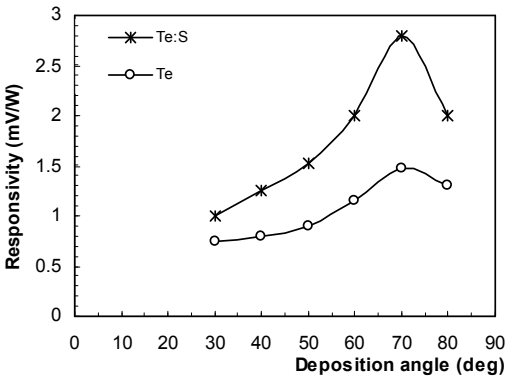

Fig. (16): The responsivity as a function of deposition angle for the Te:S and Te thin film detectors after being exposed to a ruby laser pulses

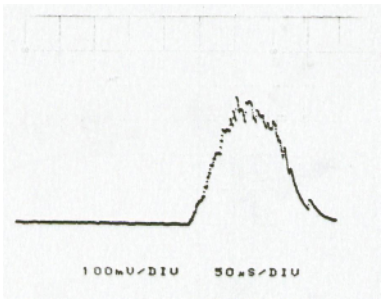

Fig. (17): The detected output pulse from thin Te:S film deposited at 70° after being exposed to a ruby laser pulse

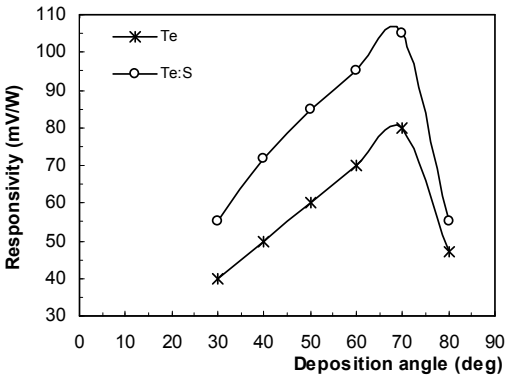

Fig. (18): Responsivity vs. deposition angle for the Te:S and Te thin film detectors after being exposed to Nd:YAG laser pulses

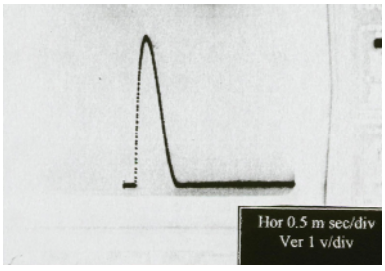

Fig. (19): Output pulse from Te:S thin film detector when θ=60° and θ=70° after being exposed to Nd:YAG laser pulses

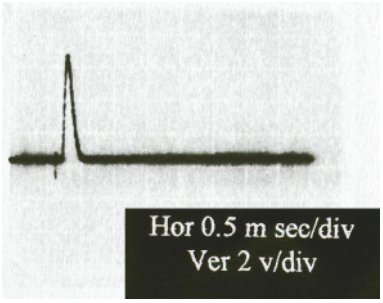

Fig. (20): Output pulse from Te:S thin film detector deposited at θ=70° after being exposed to a 20mJ Nd:YAG laser pulse at room temperature

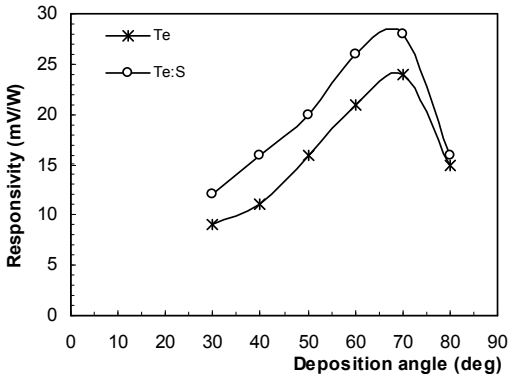

Fig. (21): Responsivity vs. deposition angle for the Te:S and Te thin film detectors after being exposed to 200ns CO_2 laser pulses at room temperature

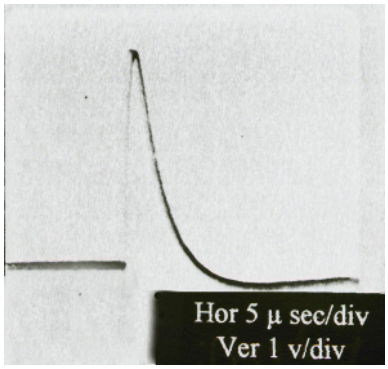

Fig. (22): CO_2 output laser pulse registered by Te:S thin film detector deposited at θ=70°

3.10 Rise Time Measurements

Figure (26) represents the rise time measurements of the Te and Te:S thin film detectors as a function of deposition angle. In general, the rise time was shorter at large deposition angles. The fastest response was 1μs for Te:S and 3μs for Te detectors when deposited at θ=60°.

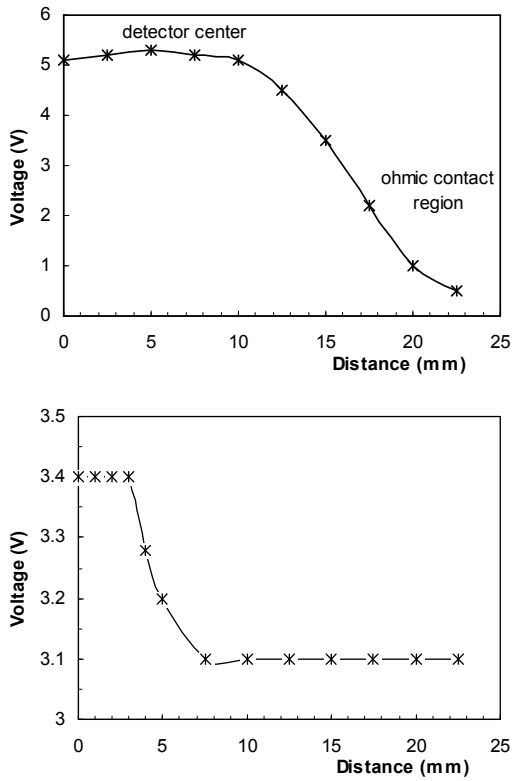

Fig. (23): Output voltage from Te:S thin film detector after the incidence of Nd:YAG laser pulses, as a function of the distance from the ohmic contact

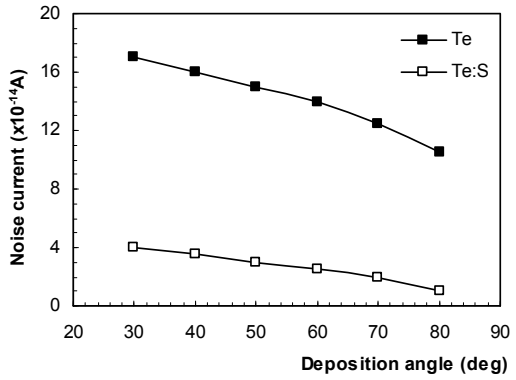

Fig. (24): Noise current variation with deposition angle for Te:S and Te thin film detectors

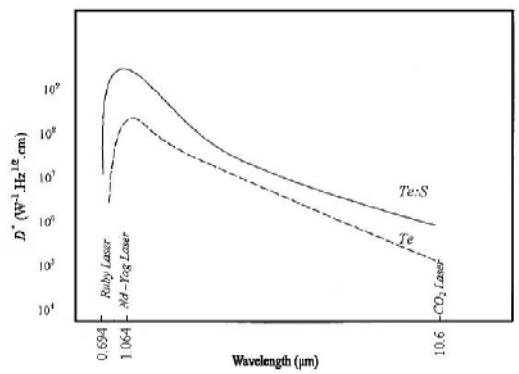

Fig. (25): Specific detectivity vs. wavelength for thin film Te:S and Te detectors at room temperature

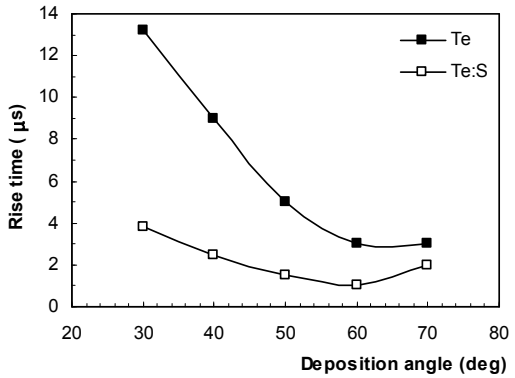

Fig. (26): Response time vs. deposition angle for Te:S and Te thin film detectors

5. Conclusions

The nanostructural characteristics of obliquely deposited thin Te:S film detectors were introduced as functions of the deposition angle. These characteristics raised after thermal treatment. The best results of the optical and electrooptic characteristics were obtained at deposition angle of 70°. The thin Te:S film detector had responded to a wide spectral range (0.4-12)μm and proved useful as laser detectors. Their responsivity to incident laser spot was the same at any point of the sensitive area especially when prepared with a thickness of 350nm. They are extremely cheap, relatively fast (1μs) and large area (10mmx60mm) laser detectors with specific detectivities of $3x10^9$ $W^{-1}.Hz^{1/2}.cm$ at the visible & NIR spectrum and 10^6 $W^{-1}.Hz^{1/2}.cm$ at 10.6 μm.

References

[1] D.R. Biswas, *J. Mater. Sci.*, 21 (1986) 2217.

[2] G. Hass, **"Physics of Thin Films"**, Academic Press (NY) (1963).

[3] M.F. Al-Kuhaili et al., *J. Phys. D: Appl. Phys.*, 35 (2002) 910-915.

[4] B. Chakrabarti et al., *J. Appl. Phys.*, 51(8) (1980) 411.

[5] N. Nakhoodkin, A. Shalder and A. Bardamid, *Thin Solid Films*, 34 (1976) 21.

[6] A.G. Dirks and H.J. Leamy, *Thin Solid Films*, 47 (1977) 219.

[7] P. Bhardwaj, P.K. Shishodia and R.M. Mehra, *J. Optoelectron. Adv. Mater.*, 3(2) (2001) 319-322.

[8] J.K. Cho et al., *Jpn. J. Appl. Phys.*, 27(2) (1988) 240.

[9] W.F. Wefston et al., *J. Vac. Sci. Technol.*, 15(1) (1978) 54.

[10] D-X. Ye, D-X. et al., *Nanotechnology*, 15 (2004) 817-821.

[11] K-S. Moon and S-C. Shin, *J. Appl. Phys.*, 79(8) (1996) 4991-4993.

[12] M. Suzuki and Y. Taga, *J. Appl. Phys.*, 40 (2001) L358-L359.
[13] T. Hashimoto et al., *J. Phys. Soc. Japan*, 41(4) (1976) 1433.
[14] N.G. Nakhoodkin and A.I. Shalder, *Thin Solid Films*, 10 (1972) 109.
[15] M.J. Peterson and F.H. Cocks, *J. Mater. Sci.*, 14 (1979) 2709.
[16] I.S. Athwal, J. Kaur and R.K. Bedi, *Thin Solid Films*, 162 (1988) 1.
[17] S. Chaudhuri, Chakrabarti and A.K. Pal, *Thin Solid Films*, 82 (1981) 217.
[18] A. Devos and J. Aerts, *Thin Solid Films*, 46 (1977) 223.
[19] R. Marshal, L. Atlas and T. Putner, *J. Sci. Instrum.*, 43 (1966) 144.
[20] F. Warkusz, *Thin Solid Films*, 52 (1978) L9.
[21] B. Goldstein and I. Pensak, *J. Appl. Phys.*, 40 (1959) 155.
[22] R.J. von Gutfeld, *J. Appl. Phys.*, 47 (1976) 3435.
[23] G.C. Bhar and R.C. Smith, *Phys. Stat. Solid. (a)*, 13 (1972) 157.
[24] M. Jycomonji, *Jpn. J. Appl. Phys.*, 35 (1966) 6592.
[25] J.W. Patten, *Thin Solid Films*, 63 (1979) 121.

This article was reviewed at The Department of Materials Sciences and Engineering, John Hoking University, U.S.A, and School of Applied Sciences, University of Technology, Baghdad, IRAQ

During the first semester of 2006

January 08 – 11	9th Regional Arab World Renewable Energy and Environment Congress , Tripoli, **Libya** Organizer: Interexpo NV Netherlands Antilles Contact: Peter Oerlemans, Fax: (+5999) 868 0197, peter@interexpo.biz
January 11 – 14	OCEANTEX 2006 , Mumbai, **India** Organizer: CHEMTECH Secretariat Fax: (+9111) 2642 7404 a_afganullah@jasubhai.com
February 27-March 2	2006 European Wind Energy Conference & Exhibition Athens, **Greece** Organizer: European Wind Energy Association Fax: (+322) 546 1944 info@ewea.org
March 09 - 11	IGU Executive Committee , Goa, **India** Organizer: International Gas Union Fax: (+45) 4517 1900 secr.igu@dong.dk
March 10 – 12	erneuerbare energien 2006 , Beblingen, **Germany** Organiser: erneuerbare energien Fax: (+49 7121) 30 16 100 redaktion@energie-server.de
March 11 – 15	17th Annual Hydrogen conference 2006 , Long Beach, CA, **USA** Organiser: National Hydrogen Association Fax: (+1 202) 223 5537 info@hydrogenconference.org
March 13 – 16	European Fuels Week , Paris, **France** Organiser: World Refining Association Fax: (+44 20) 7242 2673 marketing@theenergyexchange.co.uk

2006 . . . In the Arab Gulf Region

January 16 – 18

Middle East Petrotech 2006
Bahrain
Organizer: Overseas Exhibition Services
Fax: (+44 20) 7840 2119
mep@oesallworld.com

February 05 – 08

Middle East Electricity Exhibition & Conference
Dubai, **UAE**
Organizer: IIR Exhibitions
Contact: Sarah Woodbridge
Fax: (+971 4) 335 3526
sarah.woodbridge@iirme.com

February 27 - March 1

7th Annual Middle East Refining Conference
Dubai, **UAE**
Organizer: World Refining Association
Fax: (+44 20) 7242 2673
marketing@theenergyexchange.co.uk

March 05 – 06

Gas Arabia
Abu Dhabi, **UAE**
Organizer: The Energy Exchange Ltd
Contact: Verity Tarrant,
Fax: (+44 1242) 529 060
v.tarrant@theenergyexchange.co.uk

March 27 – 29

7th Middle East Geosciences Exhibition & Conference
Bahrain
Organiser: Overseas Exhibition Services
Fax: (+44 20) 7840 2119
geo@oesallworld.com

March 27 – 29

7th Middle East Geosciences Conference and Exhibition
Bahrain
Organiser: Overseas Exhibition Services Ltd
Fax: (+44 20) 7840 2119
aridgway@oesallworld.com

E. Rivent[1]
K. Mijama[2]
T. Sakagawa[2]
T. Kogama[2]

[1] *Department of Physical Electronics, Faculty of Science, Masaryk University, Kotlářská, Brno, Czech Republic*
e_rivent@rock.com
[2] *Research Institute of Electronics, Shizuoka University, Hamamtsu, Japan*
k.majima@rie.shizuokau.edu.jp

Growth of $In_xGa_{1-x}Sb$ Bulk Crystals by Czochralski Technique

To grow InGaSb with larger In composition, step growth process was adapted. By increasing the In composition step by step, $In_{0.1}Ga_{0.9}Sb$ single crystal of length 18mm was grown. Intensities and the FWHM values of X-ray diffraction spectrum were, respectively, 10 times larger and one third of the value, compared with the values of the crystal grown directly from GaSb seed crystal.

Keywords: *Crystal growth, InGaAs crystal, step growth, GaSb seeding*

Received: 22 September 2005, Accepted: 2 October 2005

1. Introduction

Dyring the last few years much attention has been directed to grow ternary semiconductor bulk crystals with uniform composition. Since the lattice constant can be controlled by adjusting compositional ratio, these crystals offer the possibility to reduce the problem of lattice mismatch caused at the interface between a substrate and an epilayer. Ternary semiconductors such as InGaAs [1-2], GaAsP [3], InSbBi [4] and InGaSb [5-7] have been grown at present. However, it is very difficult to grow large ternary single crystals of high quality, because there are three major problems, which must be overcome. The first is the constitutional supercooling near the growth interface in the solution. If the degree of the constitutional supercooling is large, unstable growth gets generated, and subsequently polycrystals result. The second is the compositional change in the solution during growth. Since the segregation coefficient of each component is not unity, the compositional ratio in the crystal continues to change during growth. The third is the difference of lattice constants between the seed and the grown crystal. It brings about strain in the crystal, and consequently, many dislocations are introduced.

To reduce the degree of constitutional supercooling, we have developed two new methods. One of them is the Czochralski method modified so as to introduce ultrasonic vibrations (10kHz) into the melt from the crucible bottom [8-11]. By increasing the output power of ultrasonic vibrations, $In_xGa_{1-x}Sb$ single crystal with higher In compositional ratio ($0<x<0.15$) were grown. The other method is a modified Bridgman method [12-15]. A relative motion between the growing surface and the solution can be given by rotating the growth ampoule at high speeds under covering about 60 to 90% of the growing surface with the solution.

To reduce the difference of lattice constants between GaSb seed and InGaSb grown crystal, a step growth process is adopted and the results are reported in this paper. First, $In_xGa_{1-x}Sb$ ($x=0.03$) single crystal was grown from a GaSb seed, and it was used as a seed to grow $In_{0.05}Ga_{0.95}Sb$. This process was continued to grow $In_{0.1}Ga_{0.9}Sb$. The quality of the grown crystal was compared with that of the $In_{0.1}Ga_{0.9}Sb$ crystal grown directly from GaSb seed.

2. Experiment

Figure (1) shows a schematic representation of an apparatus for Czochralski technique. A double crucible made of carbon was used to eliminate oxides from the melt surface. The outer crucible was 130mm in height, and the size of the inner crucible was 30mm in ID and 30mm in depth. A small hole was made at the bottom of the inner crucible. When the InGaSb charged material was molten, the inner crucible was pulled down by a weight hung from its edge. The melt flowed up through this small hole and the oxide slag was eliminated from the melt surface. A 25kHz rf power generator was employed to heat the crucibles which were kept in hydrogen atmosphere with hydrogen gas was flowing at a rate of 300cm^3/min. The ratio of InSb to GaSb used as source materials for growing $In_xGa_{1-x}Sb$ crystals was decided using InSb-GaSb binary phase diagram [16]. At first, a GaSb single crystal was used as a seed and $In_xGa_{1-x}Sb$

(x=0.03) was pulled in the <111> direction. The crystal rotation rate was fixed at 10rpm and the pulling speed was changed between 2.5mm/h and 5mm/h during the seeding and growth processes. By cutting the crystal 30mm from its bottom, $In_xGa_{1-x}Sb$ (x=0.03) seed crystal was obtained. $In_xGa_{1-x}Sb$ (x=0.05) single crystal was grown from $In_xGa_{1-x}Sb$ (x=0.03) seed. By repeating this process, $In_xGa_{1-x}Sb$ (x=0.1) was grown. This process is referred as step growth process. An $In_xGa_{1-x}Sb$ (x=0.1) crystal was grown directly from a GaSb seed (it is referred as direct growth process), and the quality of the crystal was compared with that of the crystal grown by step growth.

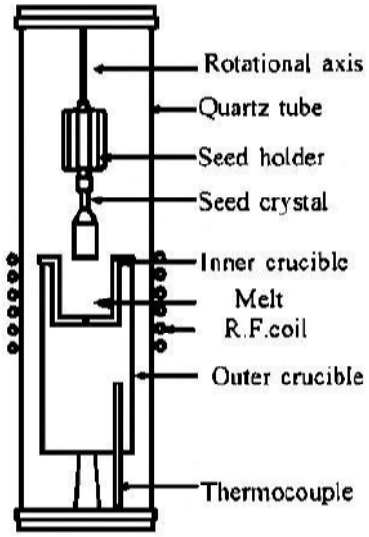

Fig. (1): Schematic representation of a Czochralski growth apparatus

Pulled crystals were cut along the growth direction so as to expose a (110) plane. Their cut surface were sufficiently polished with a 5μm-diameter alumina abrasive, and surface morphologies were observed. Electron probe microanalysis (EPMA) was done to study the compositional profiles. To measure the quality of the crystal, the X-ray intensity profile with respect to 2θ was measured using a four-crystal X-ray diffractometer.

3. Results and Discussion

At first, an $In_{0.03}Ga_{0.97}Sb$ single crystal was grown from a GaSb seed to make an $In_{0.03}Ga_{0.97}Sb$ seed. Figure (2) shows an outside view of an $In_{0.03}Ga_{0.97}Sb$ single crystal grown from a GaSb seed crystal. To prevent the dislocations from propagating into the crystal from seed necking procedure was carried out. This involved gradually reduction of diameter of the crystal until a long neck was grown. The crystal diameter was then increased to the desired size and then maintained constant. The diameter and the length of the crystal were 9mm and 73mm, respectively. By cutting the crystal 30mm from the bottom, $In_xGa_{1-x}Sb$ (x=0.03) seed crystal was constructed.

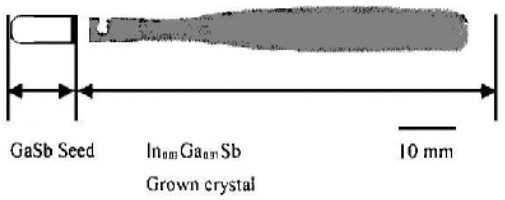

Fig. (2): Outside view of GaSb seed crystal and $In_{0.03}Ga_{0.97}Sb$ grown crystal

Figure (3) shows a (110) cut surface of an $In_xGa_{1-x}Sb$ crystal and the indium compositional profile measured along the pulling direction by EPMA. From the $In_{0.03}Ga_{0.97}Sb$ seed, $In_xGa_{1-x}Sb$ (x=0.05, 0.07, 0.09, 0.1) single crystal was grown step by step. Although the tip of the $In_{0.1}Ga_{0.9}Sb$ was polycrystalline, single crystal with the length of about 18mm was grown. The In composition was uniform in each region and its value changed step by step. This indicates that the step growth was effective to increase the In composition.

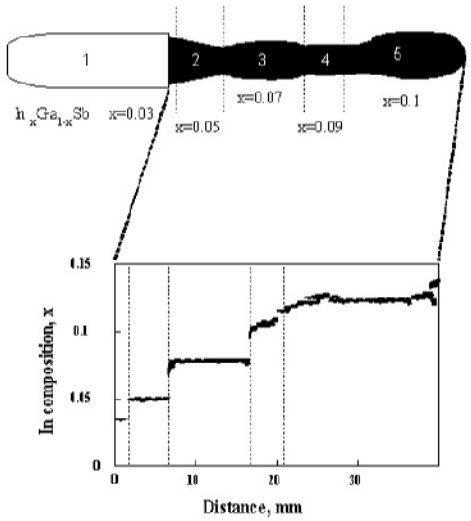

Fig. (3): (110) cut surface of an $In_xGa_{1-x}Sb$ crystal and the indium compositional profile measured along the pulling direction by EPMA

The X-ray intensity profile with respect to 2θ measured in different regions (1~5) in Figure (3) was shown in Figure (4). The diffraction angle shifted towards lower angle by increasing the In compositions. From the values of 2θ, the lattice constants were calculated by using Bragg equation. Then the value of the In composition was calculated using Vegard's law. As a result, In composition of 1, 2, 3, 4, 5 regions were calculated as 0.028, 0.052, 0.069, 0.087 and 0.098, respectively. These values coincided with those obtained from EPMA measurements.

Figure (5) shows the X-ray diffraction spectra of the $In_xGa_{1-x}Sb$ (x=0.1) single crystal grown by step growth process and direct growth process. The values of 2θ at the peaks were 41.61° in both the crystals. However, the intensity and the FWHM were quite different. Intensities of X-ray diffraction spectra and the FWHM values of the crystal grown by step growth process were, respectively, 10 times larger and one third of the value, compared with the values of the crystal grown directly form GaSb. Misfit may be considered as the reason for this. The misfit between GaSb and the $In_xGa_{1-x}Sb$ (x=0.1) was 0.63%. On the contrary, the misfit between the $In_xGa_{1-x}Sb$ (x=0.1) and $In_xGa_{1-x}Sb$ (x=0.09) was 0.063% which is 10 times smaller than that of direct growth. These results clearly indicated that the step growth was very effective to improve the quality of InGaSb ternary crystals.

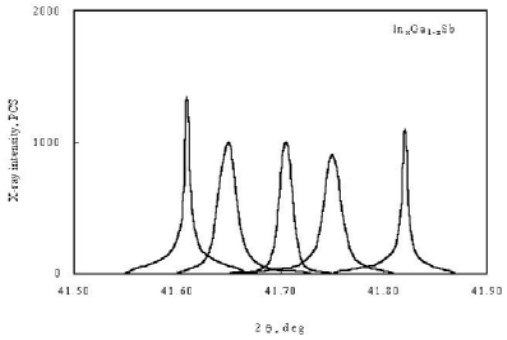

Fig. (4): The X-ray intensity profile with respect to 2 θ measured in the regions (1-5) in Figure (3)

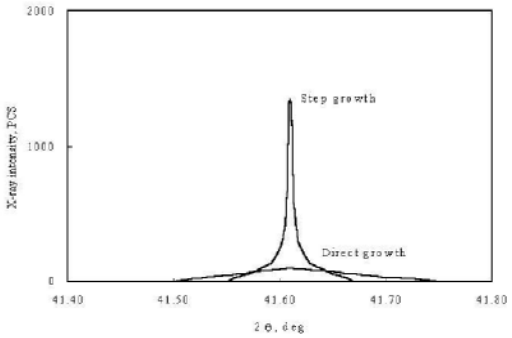

Fig. (5): The X-ray diffraction spectra of the $In_xGa_{1-x}Sb$ (x=0.1) single crystal grown by step growth process and direct growth process

4. Conclusions

A step growth process was adopted to grow $In_xGa_{1-x}Sb$ (x=0.1). By increasing the In composition step by step, $In_{0.1}Ga_{0.9}Sb$ single crystal of length 18mm was grown. To compare the quality of the crystal grown by step growth, an $In_xGa_{1-x}Sb$ (x=0.1) crystal was grown directly from a GaSb seed. Intensities and FWHM values of X-ray diffraction spectrum of the crystal grown by step growth process were, respectively, 10 times the values of the crystal grown directly from GaSb.

References

[1] T. Kusunki, C. Takenaka and N. nakajima, *J. Cryst. Growth*, 112 (1991) 33.
[2] N. Nakajima, T. Kusunuki and C. Takenaka, *J. Cryst. Growth*, 113 (1991) 485.
[3] T. Hibiya et al., *J. Electrochem. Soc.*, 134 (1987) 981.
[4] B. Joukoff and A.M. Jean-Louis, *J. Cryst. Growth*, 12 (1972) 169.
[5] K.J. Bachmann et al., *J. Electron. Mater.*, 9 (1980) 445.
[6] A. Watanabe, A. Tanaka and T. Sukegawa, *Jpn. J. Appl. Phys.*, 32 (1993) L793.
[7] A. Tanaka et al., *J. Cryst. Growth*, 135 (1994) 269.
[8] T.Tsuruta, Y. Hayakawa and M. Kumagawa, *Jpn. J. Appl. Phys.*, 27 (1988) 47.
[9] T.Tsuruta, Y. Hayakawa and M. Kumagawa, *Jpn. J. Appl. Phys.*, 28 (1989) 36.
[10] T. Tsuruta et al., *Jpn. J. Appl. Phys.*, 31 (1992) 23.
[11] M. Kumagawa et al., *Jpn. J. Appl. Phys.*, 31 (1992) 32.
[12] M. Kumagawa, T. Ozawa and Y. Hayakawa, *Appl. Surf. Sci.*, 33/34 (1988) 611.
[13] T. Ozawa, Y. Hayakawa and M. Kumagawa, *J. Cryst. Growth*, 109 (1991) 212.
[14] T. Ozawa, Y. Hayakawa and M. Kumagawa, *J. Cryst. Growth*, 115 (1991) 728.
[15] Y. Hayakawa et al., *J. Appl. Phys.*, 76(2) (1994) 858.
[16] G.B. Stringfellow, *J. Phys. Chem. Solids*, 33 (1972) 665.

This article was reviewed at Faculty of Chemistry, University of Louis Pasteur, Strasbourg, France, Physics Science and Research Center, Ministry of Science and Technology, Baghdad, IRAQ and the School of Applied Sciences, University of Technology, Baghdad, IRAQ.

In May 2006

3 Conferences on

Energy Sources and Techniques

May 16 - 19 2006

Wind Energy - International Trade Fair

Hamburg, Germany

Organizer: Hamburg Messe und Congress

Contact: Heiko Heiden

Tel: (+49 40) 3569 2123

Fax: (+49 40) 3569 2171

windenergy@hamburg-messe.de

May 25 - 26 2006

All-Energy Exhibition and Conference

Aberdeen, Scotland

Organizer: Media Generation Events Ltd

Contact: Kate Sudron

Tel: (+44 1423) 872 938

Fax: (+44 1423) 873 999

kate@mediageneration.co.uk

May 25 - 26 2006

4th International Conference "Pipeline Transport"

Moscow, Russia

Organizer: RPI

Contact: Vsevolod Prosvirnin

Tel: (+7095) 778 9332

Fax: (+7095) 967 0117

vsevolodp@rpi-inc.ru

Some Optical Properties of an Electrostatic Immersion Lens Using the Charge Density Method

Basma H. Hamad*
Ahmad K. Ahmad
Sabah M. Juma

Department of Physics,
College of Science,
Al-Nahrain University,
Baghdad, IRAQ
** bassma1980@yahoo.com*

A computational investigation has been carried out in the field of non-relativistic charged-particle optics using the charge density method as a boundary value problem with the aid of a personal computer under the absence of space-charge effects. This work has been concentrated on designing a two-electrode electrostatic immersion lens whose electrodes are cylindrical in shape separated by an air gap. The variable parameters of the two electrodes are the applied voltage ratio and the air gap separating them. The axial potential distribution of an electrostatic immersion lens has been computed by taking into consideration the distribution of the charge density due to the voltages applied on the two cylindrical electrodes. Potentials have been determined anywhere in space by using Coulomb's law. The optical properties of the immersion lens have been investigated under finite and zero magnification conditions.

Keywords: Charge density method, Electrostatic immersion lens, Spherical and chromatic aberration

Received: 8 June 2005, Revised: 25 August 2005, Accepted: 2 September 2005

1. Introduction

The charge density method for solving Laplace's equation was first applied in electron-optical systems by Cruise [1]. He computed the potential distribution in an axially symmetric electrostatic lens, which contained no insulators. This method is based on a simple fact that in the static case any region occupied by a conductor is free of field. If potentials are applied on the conductors (e.g. electrodes) the charges distribute themselves on the surfaces which become equipotentials. This is equivalent to forcing definite charge distribution on the electrode [2]. These charge distributions are considered to be the sources of the electrostatic potential distribution in the space surrounding the electrodes including the electrode potentials themselves. If the electrode potential can be replaced by these surface charge distributions on the electrodes, the value of the potential may be easily calculated anywhere in the space by simply using the superposition principle without employing any sophisticated computational grids as in the finite-difference or finite-element methods [3,4,5].

This method has been found to give accurate results, efficient in the use of computer time and storage, and applicable to a wide range of lens configurations. The charge density method is a particular example of Boundary Element Method (BEM). In most of the published work the lenses that are used for this purpose have been divided into N-rings; these rings are of variable width and are made narrower near the gap, where the charge density changes most rapidly [4,6]. However, in the present work the system of cylinders under applied potential has been replaced by a system of charged rings, which have the same width as illustrated in figure 1.

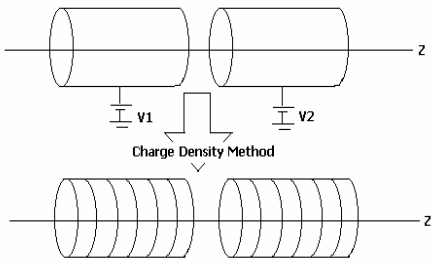

Fig. (1): Replacing a series of cylinders under applied potentials with a series of charged rings [6]

Two of the various magnification conditions that are well-known in electron optics have been taken into account in the present work, namely, the zero and the finite magnification conditions due to their resemblance to the trajectory of charged particles traversing a lens field. Under zero magnification condition the charged-

particles beam enters the lens field parallel to the optical axis, whereas under finite magnification condition the beam crosses the optical axis on both the object and image sides at a finite distance. Because of the complex nature of the present problem under investigation, the following assumptions have been made: (a) the thickness of the material from which the lenses should be constructed is negligible compared to the radii of the cylinders (b) the space charge effects are neglected in order to satisfy exactly the Laplace's equation $\nabla^2\phi=0$ and (c) Non-relativistic velocities for the accelerated charged particles have been taken into consideration.

2. Charge Density Method

The first step in the present method for calculating the axial potential distribution of a two-cylinder electrostatic lens is to find the charge density on each surface of the conducting sheets from which the lens is constructed. In the absence of dielectrics the electrostatic potential at any point in space is determined by the free surface charges on the conductors in the space [7].

The second step is, therefore, to use the determined charge density for computing the potential distribution in the space of the lens. In applying this method for equidiameter coaxial cylinders separated by a finite distance G it has been assumed that the cylinder walls have negligible thickness so that the potential in regions which are not very close to the cylinders is determined simply by the algebraic sum of the inner and outer charge sheets [8]. To solve the problem, the cylinders have been divided into N rings; each ring carries a charge Q_i (i=1,2,3,…,N) which contributes to the potentials of all the rings (see figure 2).

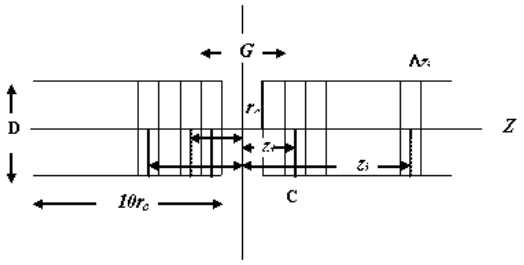

Fig. (2): Simple coaxial two-cylinder lens consisting of a large number of circular strips in order to obtain the potential distribution by CDM

The potential of the ith ring can be expressed as a combination of the contributions from all charged rings [6]. Consider the lens cylinders shown in figure 2 of radius r_c and length $10r_c$ [9]. The combined charge densities on the surfaces of the cylinders are $\sigma_i=Q_i/4\pi r_c\Delta z_i$, where Δz_i represents the width of the ith rings. If there are no other charges present then the potential at any point z in space is given by,

$$U(r_c,z)=\frac{1}{\pi\varepsilon_o}\sum_{\substack{i=1\\ j\neq i}}^{N}\sigma_i k_i K(k_i^{\,2})\Delta z_i \qquad (1)$$

Where

$$k_i=\frac{2r_c}{\left[4r_c^{\,2}+(z_i-z)^2\right]^{1/2}}$$

and $K(k^2_i)$ is the complete elliptic integral of the first kind which can be evaluated by the use of the following polynomial approximation [10],

$$K(k_i)=a_0+a_1H+a_2H^2+a_3H^3+a_4H^4+(b_0+b_1H+b_2H^2+b_3H^3+b_4H^4)\ln(1/H) \qquad (2)$$

where H=1-k_i^2 which is a dimensionless factor.

The potential V_j at a point C in figure 2 on the i[th] element is due to a constant charge density σ on each element, which is uniformly distributed around a circle of radius r_c. The potential V_j is given by the following expression [3],

$$V_j=\sum_{i=1}^{N}A_{ji}\sigma_i \qquad (3)$$

where A_{ji} is a square matrix element. The above set of equations may be reduced to the following simple matrix equation,

$$V=A\cdot\sigma \qquad (4)$$

The charge density σ is mathematically considered a column vector. In applying this procedure to the cylinder problem one may take different values of the voltage applied on the first and second electrodes, the column vector σ is then obtained by inverting the matrix A [2,11]. Hence, from equation (4),

$$\sigma = A^{-1}\cdot V \qquad (5)$$

In the present work an iterative procedure is used to get the inverse of matrix A with the aid of a computer program based on LU-Factorization method [12]. To evaluate the elements of A one needs to know the potential at the strip j caused by a uniform charge density σ_i in the strip i. The matrix element A_{ji} is given by [9],

$$A_{ji}=\frac{k_{ji}\Delta z_i}{\pi\varepsilon_0}K(k_{ji}^{\,2}) \qquad (6)$$

where

$$k_{ji}=\frac{2r_c}{\left[4r_c^{\,2}+z_{ji}^{\,2}\right]^{1/2}} \text{ and } z_{ji}=\left|\overline{z_i}-\overline{z_j}\right|$$

$\overline{z_i}$ and $\overline{z_j}$ being the mid point of the i[th] and j[th] ring respectively; they are given by

$\overline{z_i}=(z_{i+1}+z_{i-1})/2$ and $\overline{z_j}=(z_{j+1}+z_{j-1})/2$.

It should be noted that when j is equal to i the elliptic integral (equation 2) will be infinite and a singularity in the potential V is caused but not in A_{ii} itself.

3. The Trajectory Equation and Lens Aberration

The equations of motion of a charged particle traveling at a non-relativistic velocity in an electric field near the axis of a cylindrically symmetric system can be reduced to the following paraxial ray equation [13,14],

$$\frac{d^2R}{dz^2}+\frac{U'}{2U}\frac{dR}{dz}+\frac{U''}{4U}R=0 \qquad (7)$$

where U' and U'' are the first and second derivatives of the axial potential U respectively. R represents the radial displacement of the beam from the optical axis z, and the primes denote a derivative with respect to z.

The most important aberrations in an electron-optical system are spherical and chromatic aberration. Thus, the present work has been focused on determining these two aberrations for an immersion electrostatic lens operated as an objective lens. The spherical and chromatic aberration coefficients are denoted by C_S and C_C respectively. In the present investigation the values of C_S and C_C are normalized in terms of the image side focal length, i.e., the relative values of C_S/f_i and C_C/f_i are investigated as figures of merit, which are dimensionless.

The spherical aberration coefficient C_S and the chromatic aberration coefficient C_C referred to the image/object side are calculated from the following equations [10].

$$Cs=\frac{U^{-1/2}}{16R'^4}\int_{Zo}^{Zi}\left[\frac{5}{4}\left(\frac{U''}{U}\right)^2+\frac{5}{24}\left(\frac{U'}{U}\right)^4+\frac{14}{3}\left(\frac{U'}{U}\right)^3\frac{R'}{R}-\frac{3}{2}\left(\frac{U'}{U}\right)^2\frac{R'^2}{R}\right]\sqrt{U}R^4dz \qquad (8)$$

$$Cc=\frac{U^{1/2}}{R'^2}\int_{Zo}^{Zi}\left(\frac{U'}{2U}R'R+\frac{U''}{4U}R'\right)U^{-1/2}dz \qquad (9)$$

where $U=U(z)$ is the axial potential, the primes denote derivative with respect to z, and $U_i=U(z_i)$ is the potential at the image where $z=z_i$. The integrations given in the above equations are executed by means of Simpson's rule [10,15]. In the present work, equations (8) and (9) have been used for computing C_S and C_C in the image side under various magnification conditions.

4. Results and Discussion

In order to perform the computations it is assumed that a potential V_1=10 volts is applied on the left electrode of figure 2 and V_2=12 volts on the right electrode. The diameter D and length L of each cylinder shown in figure 2 are $2r_c$ and $10r_c$ respectively. The axial potential distributions at various values of the relative air gap G/D are shown in figure 3. There is a field-free region when $E(z)$=0 outside the lens boundaries. These potentials are similar in their general form.

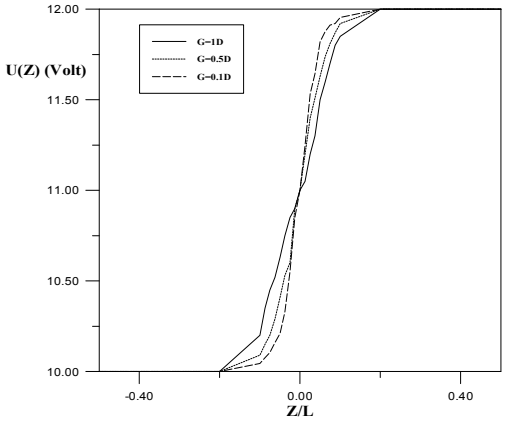

Fig. (3): The axial potential distribution on the two electrodes at various values of the relative air gap G/D

It is seen that as the relative gap ratio increases, the gradient of the curve at the region of the gap close to the higher voltage electrode increases while that close to the lower voltage electrode decreases. All curves intersect at a common point situated at the center of the air gap irrespective of the relative air gap G/D. The potential $U(z)$ at this common point of intersection (z/L=0.0) equals to 11V, which is the average of the potentials applied on the two electrodes. This result concerning the average is valid at all values of the applied voltage. Furthermore, this common point can be used as a criterion for the classification of the lens whether it is symmetrical or asymmetrical. Within the air gap region, the potential on the side of the lower voltage electrode penetrates the hollow cylindrical electrode and its gradient diminishes at a common point (z=-4mm) irrespective of G/D. The value of the potential at this point is equal to the voltage applied on the corresponding electrode (i.e. $U(z)$=10V). On the other hand, the potential on the side of the higher voltage electrode penetrates the hollow electrode region and its gradient diminishes at a common point (z=+4mm) where its value equals to that of the applied voltage.

The electron beam path along the electrostatic lens field under zero magnification condition and accelerating mode of operation (V_2/V_1) has been considered. Figure 4 shows the trajectories of an electron beam traversing the electrostatic lens field at various values of the voltage ratio V_2/V_1 and relative air gap G/D. Computations have shown that as the beam emerges from the lens field it converges towards the optical axis provided that V_2/V_1 does not exceed 25. In this case, the beam intersects the optical axis once.

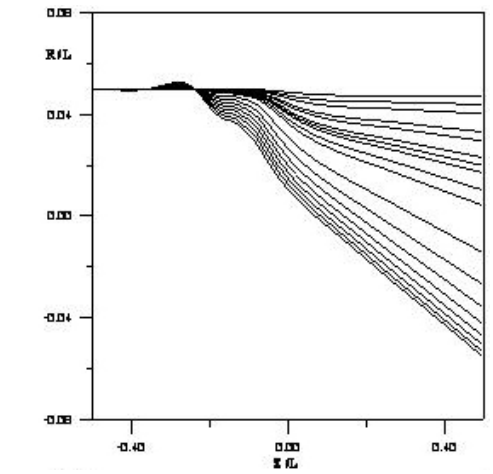

(a)

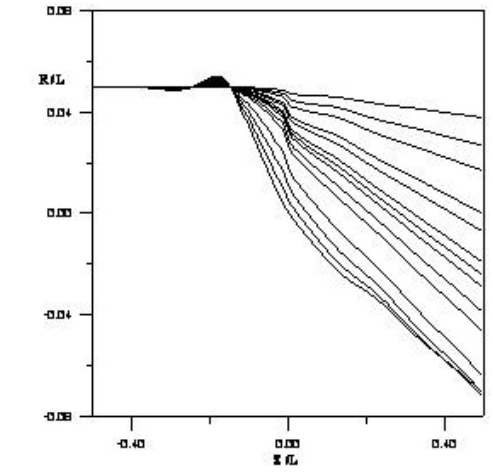

(b)

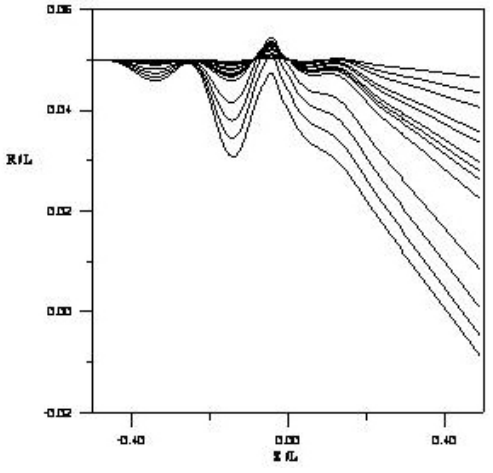

(c)

Fig. (4): The electron beam trajectory in the electrostatic immersion lens under zero magnification condition at various values of relative air gap G/D (a) G/D=0.1 (b) G/D=0.5 (c) G/D=1 for a wide range of the voltage ratio (V_2/V_1=1.2, 1.4, 1.6, 1.8, 2.0, 2.2, 2.4, 3.0, 3.5, 4.0, 6.0, 8.0, 10.0, 16.0, 18.0, 20.0 and 25.0)

However, as V2/V1 exceeds 25, the beam intersects the axis twice and hence it emerges divergent; this is due to the increase of the lens refractive power with the increase of the voltage ratio. The trajectories are similar in their general form. The effect of the relative air gap G/D (=0.1,0.5,1) on the beam trajectory has been investigated at various values of V_2/V_1 (=1.2, 1.4, 1.6, 1.8, 2.0, 2.2, 2.4, 3.0, 3.5, 4.0, 6.0, 8.0, 10.0, 16.0, 18.0, 20.0, and 25.0). The effect of the air gap is seen clearly on the beam radial displacement at various points along the lens axis. The distortion of the trajectory increases with increasing G/D particularly in the region of the left cylindrical electrode at the entrance side of the beam. Furthermore, the radial displacement of the beam at the exit side increases with increasing voltage ratio irrespective of the relative air gap. The beam is in the state of convergence at all points on the image side beyond the center of the gap. At the above mentioned voltage ratios, the trajectories have a crossover within the gap region; this crossover shifts towards the center of the lens as the gap width increases. Each trajectory represents a lens of a specific air gap G.

The aberration coefficients of each lens have been computed with the aid of the corresponding trajectory of the electron beam. Figure 5 shows the relative spherical aberration coefficient C_s/f_i of the immersion electrostatic lens as a function of the voltage ratio at various values of the relative air gap G/D under zero magnification condition.

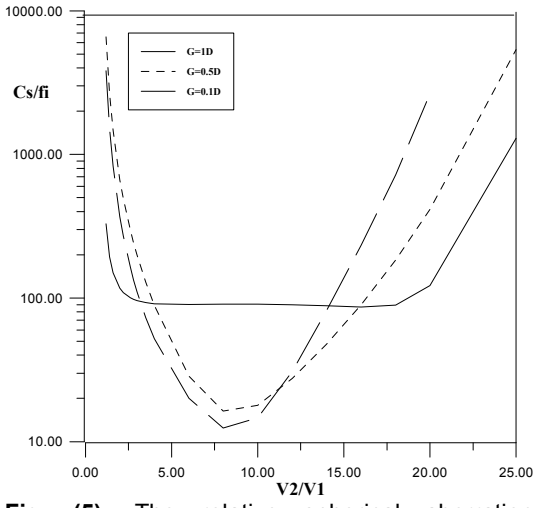

Fig. (5): The relative spherical aberration coefficient C_s/f_i as a function of the voltage ratio V_2/V_1 at various values of relative air gap

The trajectories shown in figure 4 have been used for computing the relative spherical aberration coefficients as a function of V_2/V_1 at the values of G=0.1D, 0.5D, and 1D. It is seen that C_s/f_i has a minimum value at V_2/V_1=8.0 irrespective of the value of the ratio G/D. The minimum value of C_s/f_i decreases with increasing G/D. Electron-optically, the values of $(C_s/f_i)_{min}$ are high for the above range of the ratio G/D.

Thus, this result suggests that the air gap width should be larger than the diameter of the cylindrical electrode. A plot of $(C_s/f_i)_{min}$ against G/D at V_2/V_1=8.0 indicated that the extrapolation of the curve should exceed the value of G/D=20 in order that $(C_s/f_i)_{min}$ becomes less than unity; a value accepted electron optically. For instance, in order that $(C_s/f_i)_{min}$=0.9, G/D should be equal to 20.

The relative chromatic aberration coefficient C_c/f_i has been computed as a function of V_2/V_1 at various values of G/D. Figure 6 shows that C_c/f_i increases with increasing V_2/V_1 irrespective of G/D. Low values of C_c/f_i are achieved at low values of G/D. This behavior of C_c/f_i is different from that of C_s/f_i. If one is only interested in low C_c/f_i, a relative chromatic aberration less than unity can be achieved under zero magnification conditions as shown in table (1).

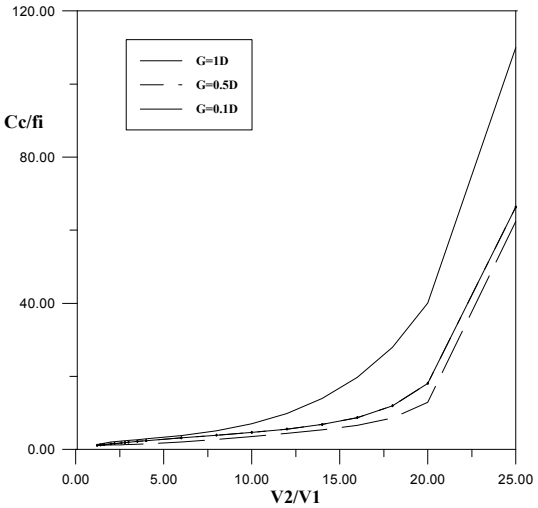

Fig. (6): The relative chromatic aberration coefficient C_c/f_i as a function of the voltage ratio V_2/V_1 at various values of relative air gap G/D

Table (1) The relative chromatic aberration coefficient at different values of G/D at V_2/V_1=1.2

G/D	C_c/f_i
0.1	0.8534
0.5	0.8871
1	0.9012

The relative image-side focal length f_i/D of the immersion lens depends on the voltage ratio V_2/V_1 as shown in figure 7 at various values of the relative air gap G/D. It is seen that f_i/D decreases with increasing voltage ratio V_2/V_1. This is due to the increase of the lens refractive power with increasing electric field within the air gap. Furthermore, the relative focal length decreases slightly as the gap width increases at any value of the voltage ratio exceeding 2.5. This is attributed to the decrease of the electric field when the air gap is widened and the applied voltage is kept constant. Figure 7 suggests that in order to achieve a low relative image-side focal length, the applied voltage ratio should not be less than 5 or exceed 20 irrespective of the air gap width.

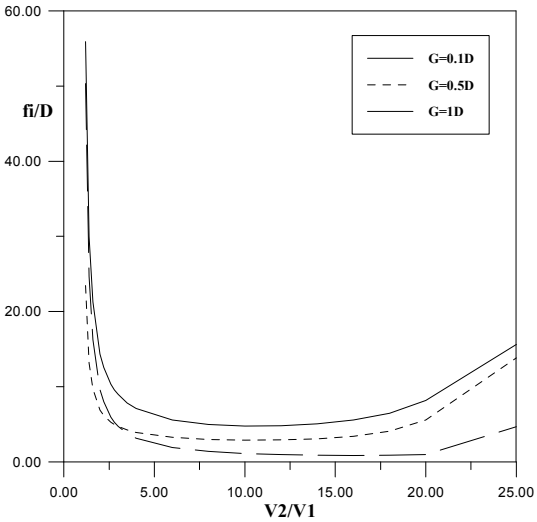

Fig. (7): The relative image-side focal length as a function of voltage ratio V_2/V_1 at various values of the relative air gap G/D

The electron beam path along the electrostatic lens field under finite magnification condition and accelerating mode of operation has been considered. Figure 8 shows the trajectories of an electron beam traversing the immersion lens field at various values of the voltage ratio V_2/V_1 and the relative air gap G/D. These trajectories have been computed under two conditions selected for the slope of the trajectory at the object position; these are R(1)=-0.52 and R'(1)=-1. The value of the trajectory slope at the object position highly affects the magnification. These trajectories are similar in their general form.

The effect of the relative air gap G/D (=0.1, 0.5,1) on the beam trajectory has been investigated at various values of the voltage ratio V_2/V_1 (=1.2, 1.4, 1.6, 1.8,2, 2.2, 2.4, 3, 3.5, 4, 6, 8, 10, 16, 18, 20, and 25). Figure 8 shows that as G/D increases the radial displacement R of the beam at the image side increases. Each trajectory represents a lens of a specific relative air gap G/D. Furthermore, the radial displacement of the beam increases with increasing voltage ratio irrespective of the gap. At the above-mentioned values of V_2/V_1, the trajectories have a crossover within the air gap region; this crossover shifts towards the center of the lens as the gap decreases.

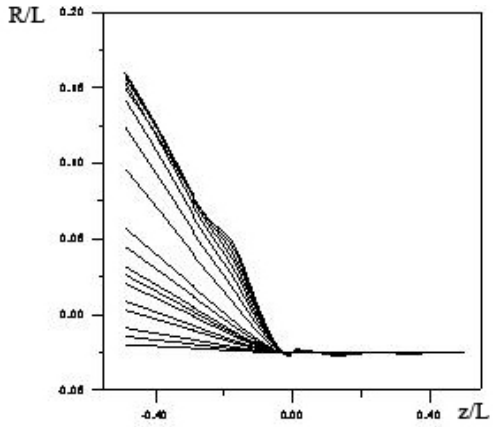

(a)

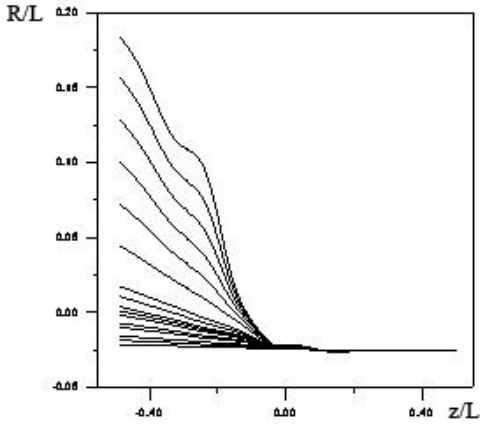

(b)

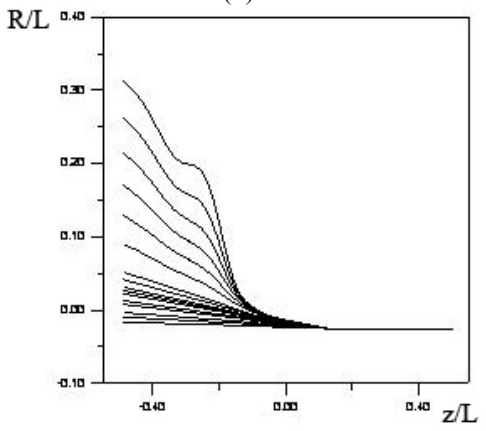

(c)

Fig. (8): The electron beam trajectory in the electrostatic immersion lens under finite magnification condition at various values of relative air gap G/D (a) G/D=0.1 (b) G/D=0.5 (c) G/D=1 for a wide range of the voltage ratio (V_2/V_1=1.2, 1.4, 1.6, 1.8, 2.0, 2.2, 2.4, 3.0, 3.5, 4.0, 6.0, 8.0, 10.0, 16.0, 18.0, 20.0 and 25.0)

The relative spherical aberration coefficient has been computed as a function of the voltage ratio V_2/V_1 for various values of the relative air gap G/D under finite magnification condition. The trajectories in figure 8 have been used for computing the relative spherical aberration coefficient at the values of G=0.1D, 0.5D and 1D. Figure 9 shows the variation of C_s/M on a logarithmic scale with V_2/V_1. The spherical aberration coefficient C_s has been normalized in terms of the magnification M since in the finite mode of operation M is more important than the focal length f although it is dimensionless. It is seen that C_s/M has a minimum value for each value of the ratio G/D.

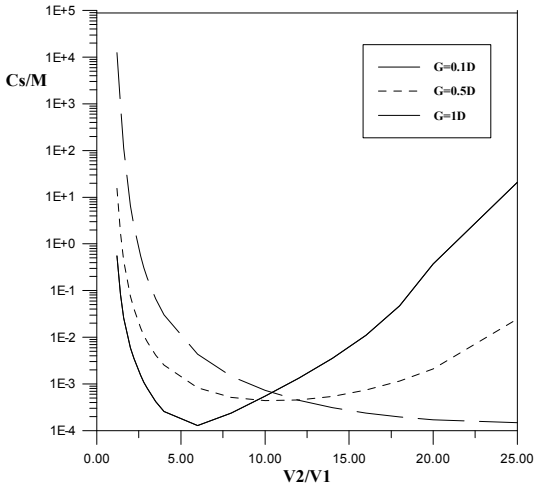

Fig. (9): The relative spherical aberration coefficient C_s/M as a function of the voltage ratio V_2/V_1 at various values of the relative air gap G/D

The minimum value of C_s/M decreases with decreasing G/D provided G/D<1. At low values of the voltage ratio V_2/V_1 the values of C_s/M are relatively low. At high voltage ratio the values of C_s/M increase for G/D=0.1and 0.5 and continues decreasing when G=1D. Thus, this result suggests that the air gap width should be less than the diameter of the cylindrical electrode if one is interested in operating the lens at low voltage ratios. The value of C_s/M that could be accepted electron-optically at a practically reasonable value of the voltage ratio is that at G<0.1D. The relative chromatic aberration coefficient C_c/M has been computed as a function of V_2/V_1at various values of G/D where both L and r_c are kept constant. Figure 10 shows that C_c/M initially decreases with increasing V_2/V_1 till a minimum value is reached.

4. Conclusions

The implementation of the charge density method on the design of electrostatic lenses appears to be an excellent tool in the field of electron-optical design. The cylindrical immersion lens that has been designed by the above method is found to have different optical properties depending upon various geometrical parameters in addition to the mode of operation. For instance under zero magnification mode of operation this lens did not exhibit acceptable properties from the electron-optical point of view. However, in the finite magnification mode of operation the lens performance was found to

be excellent. The optical properties are highly dependent on the geometrical factors of the lens such as the length of the cylinders, and the width of the air gap separating the two cylinders. Thus, one could now apply the charge density method on designing various types of electrostatic lenses.

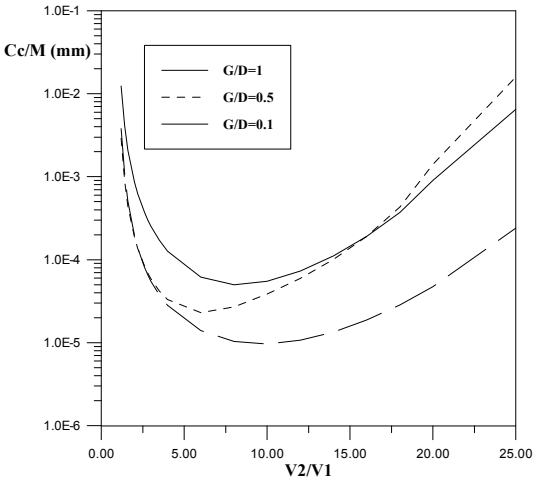

Fig. (10): The relative chromatic aberration coefficient C_c/M as a function of the voltage ratio V_2/V_1 at various values of the relative air gap G/D

References

[1] D.R. Cruise, *J. Appl. Phys.*, 34 (1963) 3477-3479.

[2] A. Renau, F.H. Read, and J.N. Brunt, *J. Phys. E: Sci. Instrum.*, 15 (1982) 347-35

[3] E. Harting, and F.H. Read, "**Electrostatic Lenses**", Elsevier (Oxford) (1976).

[4] C. Wei, and H. Rose, *J. Electron Microscopy*, 50(5) (2001) 383-390.

[5] H.A. van Hoof, *J. Phys. E: Sci. Instrum.*, 13 (1980) 1081-1089.

[6] R. Fung, "Trajectory calculation in an electrostatic positron beam using a reformulated extended charge density model" Ph.D. Thesis, Hong Kong University (Hong Kong) (1998).

[7] F.H. Read, A. Adams, and J.R. Soto-Montiel, *J. Phys. E: Sci. Instrum.*, 4 (1971) 625-63.

[8] Y.K. Wu, D.S. Robin, E. Forest, R. Schlueter, S. Anders, J. Feng, H. Padmare and D.H. Wei, *Nucl. Instrum. Methods*, A519 (2004) 230.

[9] T. Mulvey and M.J. Wallington, *Rep. Prog. Phys.*, 36 (1973) 347-421.

[10] M. Szilagyi, "**Electron and Ion Optics**", Plenum Press (New York) (1988).

[11] S. Shirakawa, H. Igarashi and T. Homma, *IEEE Trans. Magnet.*, 26 (1990) 555-558.

[12] B. Kolman, **"Introductory Linear Algebra with Applications"**, Macmillan Publishing Co. (New York) (1985).

[13] E. Bauer, *J. Phys. Condens. Mater.*, 13 (2001) 11391.

[14] B. Paszkowski, **"Electron Optics",** Ioffe Book (London) (1968).

[15] H. Muller, D. Preikazas and H. Rose, *J. Electron Microscopy*, 48 (1999) 191.

This article was reviewed at the CNRS Laboratory of Electron Optics, Toulouse Cedex, France and School of Applied Sciences, University of Technology, Baghdad, IRAQ.

Alès School of Engineering, ALÈS, FRANCE
announces to

SPECKLE06

"from grains to flowers"

13th – 15th September 2006
Nîmes – France

speckle@ema.fr

http://www.ema.fr/CMGD/speckle06/

- **Speckles, theory and fundamentals**
- **Speckle photography and digital image correlation**
- **Traditional and digital holography**
- **Holographic interferometry**
- **Speckle interferometry and shearography**
- **Phase computing and fringe patterns processing**
- **Low coherence and white light speckle interferometry**
- **Industrial and laboratory applications**
- **Measurement qualification**
- **New techniques and devices**

You could submit for participation through I.S.A.R.E.S.T. and IJAP

Subscription Coupon

FULL NAME:							
DATE OF BIRTH:		**GENDER:**		**MALE**		**FEMALE**	
DEGREE:	**PhD**		**MSc**		**BSc**		**OTHER**	
FIELD OF SPECIALTY:							
CAREER:							
INSTITUTION:							
MAILING ADDRESS:							
PHONE:				**MOBILE:**			
EMAIL:							
NO. OF COPIES:	**1**		**2**		**3**		**MORE**	
PAYMENT WAY:	**CASH**			**CHEQUE**			

To order IJAP issues, you could copy or cut this coupon and send it by mail to IJAP editor or secretary.

IRAQI JOURNAL OF APPLIED PHYSICS

" INSTRUCTIONS TO AUTHORS "

A new Iraqi specialized quarterly periodical dedicated to publishing original papers and letters in:

Applied & Nonlinear Optics	Electronic Materials & Devices	Quantum Physics & Spectroscopy
Applied Mechanics & Thermodynamics	Laser Physics & Applications	Semiconductors & Optoelectronics
Digital & Optical Communications	Plasma Physics & Applications	Solid State Physics & Applications

CONTRIBUTIONS

Contributions to be published in this journal should be original research works, i.e., those not already published or submitted for publication elsewhere, individual papers or letters to editor.

SUBMISSION OF MANUSCRIPTS

Manuscripts should be submitted to the editor at the mailing address:

Iraqi Journal of Applied Physics
Managing Editor
P. O. Box 55259, Baghdad 12001, IRAQ
irq_appl_phys@yahoo.com

Iraqi Journal of Applied Physics
Editor-In-Chief
P. O. Box 55159, Baghdad 12001, IRAQ
editor_ijap@yahoo.com

MANUSCRIPTS

Two copies with soft copy on a 3.5" diskette should be submitted to Editor in the following configuration:

- Double-spaced one-side A4 size with 2.5 cm margins of all sides
- 12pt Times New Roman font
- Letters should not exceed 5 pages, papers no more 20 pages and reviews are up to author.
- Manuscripts presented in English only are accepted.
- Authors confirm affiliations, addresses and emails. Email is necessary for correspondences.
- English abstract not exceed 150 words
- 4 keywords (at least) should be maintained on (PACS preferred)
- Author(s) should express all quantities in SI units
- Equations should be written in equation form (italic and symbolic)
- Figures and Tables should be separated from text
- Figures and diagrams can be submitted in colors for assessment and they will be returned to authors after provide printable copies
- Charts should be indicated by the software used for
- Only original or high-resolution scanner photos are accepted
- References are written in titles, full-name authors, names of publications, years, volumes, issues and pages (from-to)

PROOFS

Authors will receive proofs of papers and are requested to return one corrected hard copy with a WORD copy on a 3.5" diskette. New materials inserted in the original text without Editor permission may cause rejection of paper.

COPYRIGHT FORM

Author(s) will be asked to transfer copyrights of the article to the Journal soon after acceptance of it. This will ensure the widest possible dissemination of information.

OFFPRINTS

Authors will receive offprints free of charge and any additional offprints can be ordered.

SUBSCRIPTION AND ORDERS

Annual fees (4 issues per year) of subscription are:

- 36 000 Iraqi dinars for individuals and establishments inside Iraq.
- 50 US$ for individuals and establishments abroad.

Fees are reduced by 25% for **I.S.A.R.E.S.T.** members. Orders of issues can be submitted by contacting the editor-in-chief or editorial secretary to maintain the address of issue delivery and payment way.

THE IRAQI JOURNAL OF APPLIED PHYSICS
EDITORIAL BOARD
P. O. Box 55259, Baghdad 12001, IRAQ
Email: editor_ijap@yahoo.com

COPYRIGHY RELEASE

Iraqi Journal of Applied Physics (IJAP)

We, the undersigned, the author/authors of the article titled

……

……

that is presented to the Iraqi Journal of Applied Physics (IJAP) for publication, declare that we have neither taken part or full text from any published work by others, nor presented or published it elsewhere in any other journal. We also declare transferring copyrights and conduct of this article to the Iraqi Journal of Applied Physics (IJAP) after accepting it for publication.

The authors will keep the following rights:

1. Possession of the article such as patent rights.
2. Free of charge use of the article or part of it in any future work by the authors such as books and lecture notes without referring to the IJAP.
3. Republishing the article for any personal purposes of the authors after taking journal permission.

To be signed by all authors:

Signature:……..date: ……..
Printed name: ……..
Signature:……..date: ……..
Printed name: ……..
Signature:……..date: ……..
Printed name: ……..

Correspondence address:

……

……

Telephone:……Fax:……..email: …….

Note: Please complete and sign this form and mail it to the below address with your manuscript

The Iraqi Journal of Applied Physics,
P. O. Box 55259, Baghdad 12001, IRAQ
Email: irq_appl_phys@yahoo.com ***or*** editor_ijap@yahoo.com
Mobile: +9641-7901274190